PORE-TO-CORE SIMULATIONS OF FLOW WITH LARGE VELOCITIES USING CONTINUUM MODELS AND IMAGING DATA[*]

MALGORZATA PESZYNSKA [†] AND ANNA TRYKOZKO [‡]

Abstract. We consider computational modeling of flow with small and large velocities at porescale and at corescale, and we address various challenges in simulation, upscaling, and modeling. While our focus is on voxel-based data sets from real porous media imaging, our methodology is verified first on synthetic geometries, and we analyze various scaling and convergence properties. We show that the choice of a voxel-based grid and REV size can lead up to 10-20% difference in calculated conductivities. On the other hand, the conductivities decrease significantly with flow rates, starting in a regime usually associated with the onset of inertia effects. This is accompanied by deteriorating porescale solver performance, and we continue our experiments up until about 50% reduction in conductivities, i.e., to Reynolds number just under 1. To account for this decrease, we propose a practical power-based fully anisotropic non-Darcy model at corescale for which we calculate the parameters by upscaling.

Key words. flow in porous media porescale simulations Navier-Stokes equations upscaling non-Darcy flow inertia effects anisotropy Forchheimer model convergence

AMS subject classifications. MSC 76S05, 76M45, 76M50

1. Introduction. It is well known that in the steady linear laminar regime, the fluid momentum in saturated flow in porous media is described well by Stokes model and at corescale by Darcy flow model. Large flow rates at which the linear models are not adequate arise in the vicinity of wells, e.g., in gas reservoirs, as well as in large porosity porous media such as gravel beds, unconsolidated sediments, or fibrous porous media. The models used in nonlinear laminar regime are Navier-Stokes equations at porescale and non-Darcy models at corescale. However, non-Darcy models at corescale have not been unequivocally identified and the range of parameters for those that have been proposed varies substantially. In this paper we link the porescale and corescale by upscaling and propose a practical way to identify a non-Darcy model and its parameters which fit well the computational data.

Various computational strategies can be used to simulate flow at porescale and then to upscale the results to calculate corescale model parameters, e.g., Darcy conductivities. Such simulations and calculations are very useful since they can be used as non-destructive *in-silicio* experiments for porescale geometries dynamically changing due to deformation or chemical deposition, and thus can be used as a predictive tool in various environmental, energy-related, and industrial applications. In addition, given imaging data, the computational experiments have the ability to calculate some properties of the porous media which are hard to obtain experimentally, such as hydraulic radius, or off-diagonal components of anisotropic tensors. However, one has to assess the accuracy and efficiency of the computational experiments the same way as it is done for physical experiments, and one has to be at least aware of the computational errors that necessarily arise in porescale simulations and in upscaling.

[†]Department of Mathematics, Oregon State University, Corvallis, OR 97330, USA (mpesz@math.oregonstate.edu)

[‡]Interdisciplinary Centre for Mathematical and Computational Modeling, University of Warsaw, Pawinskiego 5a, blok D, 02-106 Warsaw, Poland (A.Trykozko@icm.edu.pl)

For the problem of interest in this paper, the modeling error has to be considered as well.

Our approach to identify non-Darcy models is to use traditional continuum solvers for porescale simulations with careful control of the quality of results. We then follow with a pore–to–core upscaling methodology that we introduced in [34]. In [36, 33] we applied it to synthetic 2D periodic geometries and carried out a suite of scaling and convergence studies. Using a range of large flow rate simulations we also calculated parameters of the quadratic isotropic non-Darcy model, i.e., Forchheimer model. In [33, 35] we also speculated on the form of anisotropic non-Darcy flow model. Because various authors indicated a qualitative difference between the 2D and 3D non-Darcy models, we did not conclude our studies until we had enough realistic porescale data to work with.

In this paper we assess the applicability of the methodology from [33] to complex 3D geometries based on voxel imaging data of real pore samples. The original voxel data sets are large enough that only their reduced versions are amenable to computations but we test the influence of reductions. We also construct a slew of 3D synthetic geometries for testing, important scaling studies, and convergence analyses.

We work under the assumption of linear or nonlinear laminar regime and of steady flow. The steps in simulations involve setting up the computational grid, and boundary conditions for the flow. These determine accuracy and solver performance and are delicate especially at large flow rates. We also test whether the use of body-fitted unstructured grids for voxel data versus the use of structured grids has any significant advantages.

After porescale simulations are completed, the results are upscaled to deliver data for the proposed non-Darcy model that can be used at corescale. We show that the quadratic Forchheimer model is not in general adequate as its coefficients vary with flow rates. Next we propose a practical non-Darcy model. We choose, among various possibilities, a practical power model for which parameters can be easily calculated. We also clearly identify the flow rate at which validity of the Darcy model ends.

Because of the enormous complexity of porescale geometries, it is crucial to find practical ways to cut down computational cost without significant impact on the accuracy of upscaled quantities. As concerns upscaling, it makes sense only over a large enough Representative Elementary Volume (REV)[9], and this is especially important for data sets with a large variety of geometric features. However, for periodic media, we provide a comparison of *one-pore* and *many-pore* geometries since it suffices to consider a very small REV of one periodicity cell only. While this approach cannot be generalized to general non-periodic media, it provides a bridge between studies over one-pore and many-pore geometries.

The paper is organized as follows. In Section 2 we recall known models for non-linear laminar flow at porescale and corescale and we overview related literature. In Section 3 we provide information about porescale data sets, and upscaling algorithm. In Section 4 we give detailed results of simulations, and their complexity is discussed in Section 5. The paper concludes in Section 6.

In the paper we use metric unit system unless otherwise explicitly stated.

2. Literature review. Porescale flow simulations conducted in order to identify macroscopic properties of porous medium were undertaken in various studies. Discrete modeling using Lattice Boltzmann or pore network modeling has been very popular, and it has advantages in several situations; see recent works [14, 5, 41] and

references therein. In particular, pore network models have relatively small computational complexity since they do not aim to resolve the details of porescale pressures or velocities in the pores or pore throats. In contrast, Lattice Boltzmann (LB) models [45] provide these details. However, in complex geometries they require very small time steps and thus are very computationally expensive.

In contrast, continuum models, i.e., direct discretizations of Stokes or Navier-Stokes equations, provide approximate values of pore pressures and velocities, but require a robust solver and a good grid with many degrees of freedom leading to considerable computational complexity. While many proof-of-concept results have been obtained with continuum models for 2D synthetic geometries and linear laminar flows, large flow rate simulations in complex pore geometries have been much less common. As alternative, Lagrangian particle methods such as Smoothed Particle Hydrodynamics (SPH) [47, 46] can be used but these suffer from similar time step constraints as LB as well as require care in handling the no slip condition on pore boundaries; thus they are mostly effective for dynamically changing geometries. Another Lagrangian-based approach combined with immersed boundary method of [43] was shown to be very sucessful for low velocity simulations. An elegant approach related to the immersed interfaces [43] which takes advantage of fictitious domain methods is compared to the use of body-fitted grids for synthetic packed beds in [18], but we are not sure if the body-fitted grids are needed for voxel-based data.

For small flow rates the recent work on porescale simulations in [52, 31, 51, 2] focused on concerns of accurate representation of pore geometries for a given numerical approximation technique. For Finite Element or Finite Volume solvers, unstructured tetrahedra-based meshes can be used to accurately describe geometries of porous structures ranging from synthetically generated spheres through granular media to complex structures representing sandstone [52]. On the other hand, Finite Difference Method can use structured grids which fit in a natural way the given voxel-based geometries provided by micro-imaging [28, 26]. Generally tetrahedral meshes represent very well arbitrary synthetic porescale geometries with a relatively low number of computational degress of freedom. However, they are not as effective for geometries arising from voxel-based data since they require tremendous mesh generation efforts or they require some transformation of the original geometry. Given that voxel data from imaging is obtained as an approximation of the true geometry, there is a concern that investments in mesh generation for such data are not justified.

In this paper we are interested in linking the porescale flow simulations with continuum models to find effective, i.e., upscaled, models at corescale, across a large range of flow rates. Theoretical work on upscaling Stokes flow to determine parameters of a Darcy model at corescale was inspired by Tartar's analysis in [48] who used homogenization theory for periodic porescale geometry. In other works [7, 9, 24] the upscaling Stokes→Darcy was achieved for general geometries by volume averaging.

On the other hand, much work was denoted to theoretical, experimental, and numerical issues as concerns modeling of flow with large flow rates at corescale. We refer the reader for background to [17, 25] and to the references in [22, 44, 34, 36, 33]. Theoretical models for flow with inertia were developed as early as in [19, 16] for scalar or 1D flow, and were later considered in [30, 20, 23, 13, 10]. The scalar inertia model was extended to multidimensional isotropic media in [16, 7, 42, 15, 8]. However, the form of non-Darcy's law for general anisotropic 2D and 3D media has not been unequivocally identified, and there exist controversies and inconsistencies as concerns the form and measurements of the essential terms. In particular, in [44] we reported

on a wide range of correlations for the inertia coefficient β and the fact that they usually overpredict the experimental values. Based on 2D simulations, in [35] we observed that even the form of the model is under question. In this paper our goal is to identify a practical model for inertia with anisotropy for which coefficients are easily calculated from porescale simulations; it turns out that our model extends/includes as a special case the model from [9] and many results quoted above.

To our knowledge, our work on using continuum models for porescale simulations in inertia regime and geometries with anisotropy has been preceded by relatively few works. In [3, 20, 21] Forchheimer model was found adequate for a range of flow rates up to a certain transition zone which is narrower in 3D flows compared to that in 2D flows. In [29, 12] Finite Element based porescale studies for periodic 2D and 3D domains were conducted, and for very large flow velocities a turbulence model was applied in [29]; these works conclude that no general upscaled model exists for a large range of flow rates. On the other hand, anisotropy was taken into account in low flow rate studies in [26, 28]. At the same time, anisotropic media are hard to study experimentally [38] from which follows the aforementioned advantage of *"in-silicio"* experiments.

In this paper we continue our computational study of flow with large flow rates in realistic porescale geometries and propose a practical upscaled anisotropic non-Darcy model for which coefficients are computed readily from porescale simulations.

2.1. Flow models at porescale and corescale. At porescale, we assume that the pore pressures p and velocities v satisfy the stationary[1] Navier-Stokes equations

$$\rho v \cdot \nabla v - \mu \nabla^2 v = -\nabla p, \ \ x \in \Omega_F, \tag{2.1}$$

$$\nabla \cdot v = 0, \ \ x \in \Omega_F. \tag{2.2}$$

Here we have assumed that there are no volume forces and, in particular, we ignored gravity. When overall flow rate is small, we approximate (2.1) by the Stokes equation

$$-\mu \nabla^2 v = -\nabla p, \ \ x \in \Omega_F. \tag{2.3}$$

Now recall Darcy's law which is written for macroscopic pressures P and velocities V

$$V = K \nabla P = \frac{k}{\mu} \nabla P, \ \ x \in \Omega, \tag{2.4}$$

where the conductivity $K := \frac{k}{\mu}$ and k is the absolute permeability. The equation (2.4) is coupled with $\nabla \cdot V = 0$, and has been proven [10, 8] to be the macroscopic limit of (2.3). Note that (2.3) and (2.4) hold in Ω_F and Ω, respectively.

For large flow rates it is known that (2.4) must be extended so it can correspond properly to the momentum conservation for larger flow rates at porescale (2.1). A scalar extension, the Forchheimer model [19] extends (2.4) with the term $\beta|V|V$ which provides the quadratic correction to resistivity

$$(1 + \beta|V|)V = \beta|V|V + V = -K\nabla P \tag{2.5}$$

Both K and β depend only on the geometry of porous medium. When different fluids are involved, it makes sense to recognize that $\beta = \frac{\bar{\beta}}{\nu}$ and $K = \frac{k}{\mu}$, and to calculate the absolute permeability k and absolute inertia parameter $\bar{\beta}$.

---

[1]One can also use the non-stationary Navier-Stokes model but for the range of flow rates in this paper it gives results nondistinguishable from the stationary approximation

Mathematically equivalent to (2.5) is the notion of flow rate dependent resistivity $\kappa^{-1}(V) = K^{-1} + \tilde{\beta}I|V|$ of the porous medium which is linear in $|V|$; this notation common in petroleum industry was used in [22, 34, 33], where instead of (2.5) we write

$$\kappa^{-1}(V)V = -\nabla P. \tag{2.6}$$

In (2.6) the coefficient $\tilde{\beta} = K^{-1}\beta$ is, however, of order $O(K^{-1})$ and has a large magnitude of $O(10^{11})$ [17], which makes $\tilde{\beta}$ a suspect in any model fitting efforts. Thus in this paper we extend (2.5) instead of (2.6).

There exists extensive theoretical work in [50, 30, 39, 40, 10, 27, 23] devoted to various forms of non-Darcy law extending (2.6); see also [6] for theory combined with some simulations. However, these results are largely inconclusive as concerns a practical non-Darcy model that can be implemented in a corescale simulator.

Various sources [7, 42, 24] and our prior work in 2D [35] suggest that the model (2.5) should include corrections to the left-hand side of (2.5) of power $\alpha \neq 1$

$$(1 + \beta|V|^\alpha)V = -K\nabla P, \tag{2.7}$$

with $1 \leq \alpha \leq 3$, which includes (2.5) as a special case with $\alpha = 1$. The model (2.7) requires three parameters (K, β, α).

More generally, a correction can be formulated

$$(1 + |V|\rho(|V|))V = -K\nabla P, \tag{2.8}$$

where $\rho(\cdot)$ is some complete $\rho(r) = \beta + \gamma r$, or incomplete $\rho(r) = \gamma r$ linear polynomial, or some higher order polynomial, or a power function. Note that a constant $\rho(r) = \beta$ corresponds to Forchheimer law, i.e., an overall quadratic non-Darcy correction, while an incomplete linear polynomial model gives a cubic correction discussed, e.g., in [24], and is equivalent to (2.7) with $\alpha = 3$. The model (2.8) requires three parameters (K, β, γ), or more, if higher order polynomial is used; see the fitting experiments in Section 4.4.1. The model (2.8) will be used in this paper only for isotropic media, since its use for anisotropic media is too complicated.

A vector anisotropic version of (2.7) is readily available and can be written componentwise

$$\sum_j \beta_{ij}|V|^\alpha V_j + V_i = -\sum_j K_{ij}\frac{\partial p}{\partial x_j}. \tag{2.9}$$

In this equation both K and β are tensors, see the model in ([9], 4.3.6), for $\alpha = 1$. A further extension is possible by making α a vector, or a tensor, see Section 4.4.2.

3. Setup of simulations. The goal of our simulations is to determine the saturated conductivity K values for a wide range of flow rates. The values of K are computed using our virtual laboratory which consists of flow simulations at porescale followed by a numerical upscaling step which in turn is used to identify the best-fitting non-Darcy model.

The fluid flow model for simulations at porescale is that of stationary Navier-Stokes model (2.1)–(2.2). The data for simulations with this model are i) the (geometry of) flow domain $\Omega_F \in \mathbb{R}^3$, ii) the fluid properties, and iii) the appropriate boundary conditions. For numerical model additionally we define iv) the grid over Ω_F, and v) the solver parameters such as tolerance criteria for the iterative solver.

The numerical flow model is implemented in the ANSYS Fluent package [4] on general unstructured staggered grids. It is a finite volume-based solver [32, 49] in which the resulting set of nonlinear equations is solved by iteration. The iterations stops when desired tolerance has been achieved or if a certain prescribed number of iterations has been exceeded. Some flow simulations require many iterations and some do not complete successfully; see Section 5. The items i)-v) are described in detail in Sections 3.1–3.2.

The upscaling procedure in this paper is a volume averaging (VA) algorithm first shown in [34] and later refined in [33, 36] for 2D simulations; it is a practical implementation of standard VA definitions of K [9]. Our algorithm interprets and calculates the macroscopic gradient of pressures in a way that allows to compute K as a full tensor, see Section 3.3 for a 3D version of the algorithm. Furthermore, the algorithm leads naturally to a proper identification of non-Darcy model.

In what follows we denote by superscripts the data such as geometry or boundary conditions corresponding to particular experiments, and by subscripts their physical meaning. For example, Ω_F^{GB} denotes the fluid domain for data set GB, and $v_{in}^{GB,(j)}, V_1^{GB,(j)}$ denote, respectively, the inlet velocity for j'th flow rate and the first component of the corresponding macroscale velocity for dataset GB. We omit subscripts, superscripts, and annotations whenever the resulting more compact notation does not lead to confusion.

3.1. Geometry and grid. The porespace Ω_F in which the fluid flows is complemented by the solid matrix Ω_R so that the porous region $\Omega = \Omega_F \cup \Omega_R$. In this paper we deal with voxel-based geometry of $\Omega = \bigcup_{ijk} \omega_{ijk}$ where each cell or voxel ω_{ijk} is either entirely in Ω_F or Ω_R. For simplicity, we associate $\omega_{ijk} \equiv n_{ijk}$ where the index n_{ijk} is defined

$$n_{ijk} = \begin{cases} 1 & cell \; \Omega_{ijk} \; is \; void, i.e., : \omega_{ijk} \subset \Omega_F \\ 0 & cell \; \Omega_{ijk} \; is \; solid, i.e., : \omega_{ijk} \subset \Omega_R \end{cases} . \qquad (3.1)$$

The porosity of the porous sample Ω is thus

$$\phi := \frac{|\Omega_F|}{|\Omega|} = \frac{|\mathbf{n}_F|}{|\mathbf{n}|} = \frac{\sum_{ijk} n_{ijk}}{|\mathbf{n}|}, \qquad (3.2)$$

where $|\mathbf{n}|$ is the total number of voxels and $|\mathbf{n}_F|$ is the total number of fluid voxels.

The "voxel-ization" of the porespace is very convenient for the setup of our simulations and it allows direct import of data from imaging. However, the rock-fluid interface $\Gamma = \partial\Omega_F \cap \partial\Omega_R$ for voxel-based geometries has a particularly rugged geometry which affects the quality of fluid flow simulations. In our previous work [33] we did not use voxels but rather worked with idealized pore geometries whose boundaries were smoother than those considered here. We address the consequences of voxelization in Section 4.1.

3.1.1. Data sets. We have worked with several voxel data sets, and we summarize their properties and origin in Table 3.1. The data sets come from three different sources which we refer to as B, GB, and HS. In the Table we summarize their original properties as well as some derived quantities. For each dataset we know (or assume) the actual physical size $l := |\omega_{ijk}|$ of a voxel so that the physical size of the pore sample is $|\Omega| = l^3|\mathbf{n}|$. The data sets undergo various transformations and reductions; we denote the original data as $\Omega^0, \mathbf{n}^0, l^0$ and by $\Omega^1, \mathbf{n}^1, l^1$ the transformed data etc.

When a particular data set **D** is considered, the transformed sets are labelled **D**-0, **D**-1, and so on; the geometrical quantities are labelled with appropriate superscripts. If no voxel reduction is needed, the notation **D**-0 is simply replaced by **D**.

Now we discuss the origin of the voxel-based data sets used in this paper denoted by B, GB, and HS.

The synthetic dataset B was created as a regularly shaped $|\mathbf{n}^B| = 41 \times 41 \times 41$ matrix with a regular distribution of "sphere"-like solid shapes. The sets B1, B2, B3 were created from geometry of B in which some of the fluid cells were replaced by rock cells randomly with probability 0.1, 0.2 and 0.3, respectively; thereby the connectivity of pores and the porosity were reduced. We assumed $l^{\mathbf{D}} = 5 * 10^{-6}$ for $\mathbf{D}$ =B, B1, B2, B3. The sets B are useful in testing as well as in scaling exercises whereby they are referred to, e.g., as B1s10 etc., see Table 3.1.

The set GB obtained courtesy of Dorthe Wildenschild with $|\mathbf{n}^{GB}| = 414 \times 414 \times 300$ came from experiments in imaging glass beads. The set HS, courtesy of Brent Lindquist, with $|\mathbf{n}^{HS}| = 753 \times 753 \times 600$ came from imaging Hanford sandstone ([11], set C1), and consisted of a grain-size mixture of gravel, sand, silt, and clay.

Datasets GB and HS correspond each to a cylindrically shaped domain Ω used for porescale imaging, and the voxels surrounding the cylindrical porous sample were fluid voxels. In order to simplify the setup of multiple independent flow expriments, we cut out of each set a box of size $N_x \times N_y \times N_z$. Thus the original data sets GB and HS underwent the first reduction from $\mathbf{n}^{GB}, \mathbf{n}^{HS}$ down to $\mathbf{n}^{GB-0}, \mathbf{n}^{HS-0}$, respectively. Further, encouraged by our early experiments with HS, we considered a small cut-out HSs of HS down to $|\mathbf{n}^{HSs,0}| = 201 \times 201 \times 201$.

REV size and reductions. When given a realistic porescale data set, we want to simulate the flow in a domain as close as possible to the original one. In addition, we want to make sure that the REV is large enough so that our REV averaged quantities are reliable. At the same time, the complexity of simulations increases substantially with $|\mathbf{n}_F|$, and for some data sets it is impractical or even impossible to compute with the geometry corresponding to $\mathbf{n}_F^0$. Thus, if possible, one wants to identify some reduced geometry in a REV as small as possible, i.e., use a transformed subset of the original data in order to reduce computational time, as was done, e.g., in [41, 37].

Since the original size $\mathbf{n}^B$ of B was relatively small, no further reductions were necessary. However, while the samples GB and HS were physically small, we found it necessary to reduce $|\mathbf{n}_F^{GB-0}|, |\mathbf{n}_F^{HS-0}|$ by coarsening the original voxel grid based on a simple criterium. Consider a box of $8 = 2 \times 2 \times 2$ voxels in the original grid. It is replaced by a fluid voxel in the new coarse grid provided the number of fluid voxels in the box does not exceed 4; it is replaced by a solid voxel otherwise. For example, we create new data set GB-1 with the corresponding $\mathbf{n}^{GB-1}$ out of the original GB-0 with $\mathbf{n}^{GB-0}$. With the necessary modifications at the boundaries, this reduces the number of voxels approximately by a factor of 8, so that $|\mathbf{n}^0| \approx 8|\mathbf{n}^1|$. To preserve the physical size of Ω, we change $l^1 = 2l^0$. In some cases it was necessary to proceed with another reduction step to obtain $\mathbf{n}^2$ from $\mathbf{n}^1$.

Clearly the process of reduction alters the geometry and the connectivity of porespace. In particular, the coarsening–reduction step usually leads to a slightly increase in porosity as compared to original data. We study the related effects along with grid size effects in Section 4.

Looking at the physical size of Ω for each data set we see that it is was of the order of around $(0.1cm)^3$ which is quite small compared to the range $[10cm - 1m]^3$ usually considered to be the Darcy scale. Fortunately the volumes we were working with

proved to be large enough with respect to their geometrical structure and this was sufficient for the volume averaging procedures from this paper. This is not always the case; another data set from imaging of volcanic tuff, also courtesy of Dorthe Wildenschild, could not be used for pore-to-core upscaling and is not analyzed in this paper.

3.1.2. Removal of dead-end pores. Given the original or reduced pore geometry $\mathbf{n}$, we need to remove the dead-end pores, i.e., pores or groups of pores completely surrounded by rock grains which do not take part in fluid flow simulation. It is relatively easy to determine the list of such pores using a simple iterative percolation algorithm which we describe below.

Consider one of our computational experiments in which flow is from left to right. We first set $p_{ijk}^{(0)} = n_{ijk}$ for all voxels. We then seed the fluid cells on the left face of the sample, i.e. with $j = 1$, with some unique numbers greater than 1, e.g, with an index $p_{i,1,k}^{(0)} = (i-1) * N_z + k + 1$, corresponding to the (i,k)'th cell on the left face. Next we iterate $it = 0, 1, 2, \ldots$ looping over those $p_{i,j,k}$ which are positive and we set in the new iteration

$$p_{i,j,k}^{(it+1)} = \max(p_{i,j,k}^{(it)}; p_{i-1,j,k}^{(it)}, p_{i+1,j,k}^{(it)}, \tag{3.3}$$
$$p_{i,j-1,k}^{(it)}, p_{i,j+1,k}^{(it)}, p_{i,j,k-1}^{(it)}, p_{i,j,k+1}^{(it)}).$$

For a cell on the boundary, the indices outside the region are eliminated. Algorithm (3.3) typically completes in

$$O(max(N_x, N_y, N_z))$$

iterations; see Table 3.1.

The porespace has connectivity, i.e., percolates, if at least one of the nodes (i, N_y, k) on the right face of sample satisfies that $p_{i,N_y,k}^{(it)} > 1$. If we are only interested in whether the sample percolates, the algorithm completes quickly. However, to isolate the dead-end pores we have to continue iterations until $p^{(nit)}$ does not change anymore. At this point we identify and remove those pores denoted by $\Omega_{dead} \subset \Omega_F$ that have not been visited, i.e., for which $p_{i,j,k}^{(nit)} = 1$ and there is no path connecting it to any of the cells $n_{i,N_y,k}$ on the right face. Then we set $\Omega_F^{eff} := \Omega_F \setminus \Omega_{dead}$, with the obvious notation of $|\mathbf{n}^{eff}| = \sum_{\omega_{ijk} \in \Omega_F^{eff}} n_{ijk}$. Table 3.1. We also recompute the porosity ϕ^{eff} and from that point on, we only work with the effective fluid space Ω_F^{eff}.

With a little extra effort we can compute from $\mathbf{n}$ some parameters characterizing Ω_F, e.g., its specific surface area Σ_{vs} defined as the solid total area per volume of the solid matrix. The estimate of mean grain size $d_{char} = 1/\Sigma_{vs}$ is then available as suggested in ([9], p119); this value is reported in Table 3.1. We use d_{char} in Carman-Kozeny correlation calculations and in the estimates of Reynolds numbers in Section 4. From geometric inspection of the data sets one can also infer crude estimates of d_{char} but they are typically far off those in Table 3.1. Alternatively, in ([9], p146) it is proposed to use instead of d_{char} the hydraulic radius d_h, i.e., the ratio of void volume to the solid total area. This is also easily computed, see Table 3.1.

3.1.3. Grid. Given $\Omega_F \equiv (\mathbf{n}, l)$, the next step is to create a quadrilateral (hexahedral) grid for flow simulations covering Ω_F.

We choose the grid to be a union of regular hexahedral cells of size h^3 into which each of the fluid voxels in Ω_F is divided. While the grid cells can be 'IJK' numbered

dataset	N_x	N_y	N_z	$|\omega^{dead}|$	nit	ϕ	ϕ_{eff}	$10^6 l$	$10^6 d_{char}$	$10^6 d_h$
B	41	41	41	0	81	0.7243	0.7243	5	1.76	4.62
B1	41	41	41	9	82	0.6238	0.6237	5	2.36	3.91
B1s10	41	41	41	9	*	0.6238	0.6237	50	23.6	39.1
B1s100	41	41	41	9	*	0.6238	0.6237	500	231	391
B2	41	41	41	62	82	0.5253	0.5244	5	3.07	3.38
B3	41	41	41	160	82	0.4228	0.4205	5	4.11	2.98
GB-0	280	280	300	1574	589	0.3587	0.3586	17	-	-
GB-1	141	141	150	281	294	0.3746	0.3745	34	116.95	70.03
GB-2	71	71	75	49	147	0.4003	0.4002	68	118.95	79.37
HS-0	520	520	600	60745	1232	0.3571	0.3568	3.97	-	-
HS-1	257	257	300	4084	570	0.3715	).3713	7.94	-	-
HS-2	129	129	150	1646	280	0.3971	0.3964	15.88	25.21	16.56
HSs-0	201	201	201	2191	405	0.3827	0.3825	3.97	20.03	12.41
HSs-1	100	100	100	885	204	0.3994	0.3985	7.94	20.64	13.68
HSs-2	50	50	50	213	102	0.4300	0.4283	15.88	22.45	16.81

TABLE 3.1
Geometry information about data sets. The asterisk * denotes information repeated from a row above. Some data sets were not converted to grids due to their size, and '-' denotes information not available for these data sets.

as if they belonged to a structured grid, the grid is actually fully unstructured like any other finite element/finite volume grid. The grid generation is a fairly standard step in which one must properly account for the connectivity of the cells as well as describe all the wall surface elements, i.e., those in $\Gamma = \Omega_F \cap \Omega_R$. For large $|\mathbf{n}|$ our grid generation algorithm may need large memory and it does require noticeable computational time.

The choice of hexahedral meshes is made for convenience. It is in principle possible to create a body-fitted grid for Ω_F even if its geometrical features are already lost in the voxel data given from imaging [52]. However, we believe it is not necessary in practice, given the large additional computational burden and uncertainty this would introduce to the entire imaging-voxel-mesh-upscaling loop. Instead, we try to assess grid dependence and geometry voxelization effects as in Section 4.

We select the grid size h as follows. Assume the data set considered $\mathbf{D}$-k has undergone k reduction, i.e., the voxel size is l_k. Since in $\Omega^{\mathbf{D}-k}$ several channels of width of one voxel may be present, in order to properly resolve the details of fluid pressure and velocities, it is necessary to use numerical quadrilateral grid size $h_m = l_k/m$ with at least $m \geq 2$ refinement levels; we denote the resulting numerical grid as $\mathbf{n}^{\mathbf{D}-k-m}$.

Whenever possible, we consider several grid refinement levels. The details shown in Table 3.2 and Section 5 give an idea of computational and data challenges and those in Section 4 the impact of grid size.

3.2. Fluid properties, boundary conditions and regimes of flow rates. As for fluid properties, we use water and methane at standard conditions with prop-

dataset	$10^6 h$	# nodes	# cells	size[Gb]
B-6	0.83	11,884,223	10,782,936	2.882
B1-2	2.50	461,334	343,896	0,104
B1-3	1.67	1,433,092	1,160,649	0,332
B1-4	1.25	3,242,968	2,751,168	0,765
B1-5	1.00	6,148,884	5,373,375	1,467
B1-6	0.83	10,408,762	9,285,192	2,505
B1s10-6	8.30	10,408,762	9,285,192	2,505
B1s100-6	83.0	10,408,762	9,285,192	2,505
B2-6	0.83	8,906,885	7,807,320	2,127
B3-6	0.83	7,272,468	6,259,464	1,723
GB-1-2	17	10,124,671	8,937,336	2,424
GB-1-3	11.33	32,833,372	30,163,509	9,115
GB-2-2	34	1,495,806	1,210,456	0,392
GB-2-3	22.67	4,727,534	4,085,289	1,276
HS-2-2	7.94	9,895,594	7,915,912	2,583
HS-2-3	5.29	31,175,674	26,716,203	8.4
HSs-0-2	1.99	27,030,028	24,847,584	7,505
HSs-1-2	3.97	3,700,921	3,188,264	0,998
HSs-1-3	2.65	11,911,799	10,760,391	3,281
HSs-2-2	7.94	542,435	428,280	0,141
HSs-2-3	5.29	1,702,074	1,445445	0,456

TABLE 3.2

Grids used in simulations denoted by **D**-*m*-*n* *where m refers to voxel coarsening level and n to grid refinement level. Not all data sets from Table 3.1 are represented here since some were too computationally complex. In addition, since the data sets B need not be reduced, B1-3 refers to grid refinement level 3 for B1, etc.*

fluid	ρ	μ	$\nu = \frac{\mu}{\rho}$
water	1000	$1.003 * 10^{-3}$	$1.003 * 10^{-6}$
methane	0.6679	$1.087 * 10^{-5}$	$1.6275 * 10^{-5}$

TABLE 3.3
Fluid properties

erties as listed in Table 3.3. We assume both fluids have constant densities and viscosities throughout all simulations, i.e., in particular incompressibility. For methane this is clearly a convenient approximation rather than reality.

The boundary conditions that work well for the fluid domain geometries Ω_F considered in this paper are as follows. We impose the wall no-slip condition $v = 0$ on $\partial\Omega_F \cap \partial\Omega_R$, and a combination of inflow and outflow condition. The external boundary $\partial\Omega_F \cap \partial\Omega$ is divided into the inflow Γ_{in}, wall no-flow Γ_0, and outflow Γ_{out} parts. We choose Γ_{in} to be part of one the faces of the rectangular box constituting Ω, and Γ_{out} to be the opposite face. There are three pairs of inflow-outflow faces, i.e. Γ_{in}–Γ_{out}, and we refer to them as 'LR' (left-right), 'BT' (bottom-top), and 'FB' (front-back). For each pair, the remaining four faces are part of Γ_0. We describe the

inflow and outflow conditions in detail below, and comment on alternatives below.

Inflow conditions.. At inflow face, we impose the constant inlet velocity condition

$$v \cdot n|_{\Gamma_{in}} = v_{in}, \tag{3.4}$$

where n, t are the normal and tangential directions to Γ_{in}, respectively, and v_{in} is some given constant. For the needs of our upscaling procedure discussed below we need at least three independent experiments with different principal flow directions for each overall flow rate $v_{in}^{(j)}$; we associate these with the pair of inflow-outflow faces 'LR','BT', and 'FB', thereby denoting the flow experiments by $v_{in,LR}^{(j)}$, etc.

Range of inlet velocities.. The range of velocities $v_{in}^{(j)}, j = 0, \ldots MAX$ for each data set corresponds to flow rates from linear laminar (Darcy) regime well into the nonlinear laminar regime (non-Darcy). These could be characterized with the nondimensional Reynolds number Re. However, its definition and use in porous media is debated and non-unique [9], and some authors suggest that its microscopic equivalent is more meaningful especially for large flow rates [5, 25]. In what follows we use the porous media Reynolds number defined as in ([9], p146, eqn 4.3.1)

$$Re = Q\frac{d_{char}}{\nu} = Q\frac{d_{char}\rho}{\mu}, \tag{3.5}$$

where d_{char} is the characteristic length scale for the model, e.g., rock grain size, such as given in Table 3.1, and $Q = \phi V$ is the macroscopic flux corresponding to the averaged macroscopic velocity V that is computed for each v_{in}.

Difficulties with accurate resolution of pressure and velocity grow substantially with flow rates. In practice we were able to run about $MAX = 20$ simulations.

Outflow conditions.. The boundary condtions at the outlet boundary Γ_{out} can be defined in several ways. The standard outflow boundary condtion [49] imposes zero diffusion flux for all flow variables. However, with outflow condition a significant recirculation may occur near complex boundaries for high flow rates, and solver performance deteriorates.

We found that a pressure outlet boundary condition in which we impose static pressure equal to 0 at Γ_{out} works better than the outflow condition, especially at high flow rates. Consequently, all the results in this paper are based on this option.

For velocities in the slow flow regime, the solver performance for both outflow and pressure outlet conditions is similar.

Alternative boundary conditions set-up.. We found the setup described above to be the most practical for the given complex geometries in 3D. Other possibilities which we explored include the use of a parabolic rather than constant inlet velocity profile as well as the use of an extended domain of flow $\Omega' \supseteq \Omega$ so that $\Omega' \setminus \Omega$ is entirely made of fluid voxels.

As concerns inlet velocity profile, for synthetic regular patterns of ellipses or circles regularly distributed within a fluid considered in [34, 36, 33], we used unstructured triangular or quadrilateral grids well representing shapes of domain boundaries. Velocities at inlet are defined to ensure parabolic profiles and this works very well especially for one-pore geometries or with few pores. However, enforcing the parabolic shape is quite cumbersome for the many-pore geometries such as GB or HS, while the impact on the solutions is not really noticeable.

Next, the idea of extending the computational domain Ω_F in the flow direction resulting in $\Omega' \supseteq \Omega$ is a common technique used to stabilize the flow for complex

flow geometries such as in arterial blood flow simulations. However, in a modest flow rate range considered here, this extension does not result in significant improvement of solver performance. At the same time, the volume of $\Omega' \setminus \Omega$ introduces additional data and computational burden for 3D simulations. For example, the size of data file for B1 nearly doubles when the original volume $|\mathbf{n}| = 41 \times 41 \times 41$ is extended by 10 voxels on each end.

Overall, the alternative boundary options work well for 2D coupled flow and transport simulations. However, we found them to be too complex for 3D simulations.

3.3. Upscaling to identify parameters of non-Darcy model. As a result of our upscaling procedure we calculate all the necessary parameters for the chosen non-Darcy model. As data for these calculations we use pressure and velocity values from flow experiments corresponding to a unique $v_{in,DIR}^{(j)}$ as described in Section 3.2.

First we average the pressure and velocity values over $\Omega_F^r := \Omega_F \cap \Omega^{REV,r} \subset \Omega_F$ whose size relative to Ω_F is dependent on a parameter $0 < r < 1/2$. We choose $\Omega^{REV,r}$ to be a box-shaped subset of Ω with the same center as Ω, and with the sides shorter than those of Ω by a factor of $1 - r$ on each side. We choose $r > 0$ to avoid including cells close to $\partial\Omega$ where possible recirculation may occur and which, for large flow rates, may lead to unstable averages.

Obtaining the averages $V_{DIR,k}^{(j)}, k = 1, 2, 3$ of velocities over Ω_F^r is straightforward. We can associate $DIR = LR, BT, FB$ naturally with the coordinate axis x_1, x_2, x_3, respectively. If the porous medium is isotropic, the vectors $V_{DIR}^{(j)}$ can only have one nonzero principal component, e.g., $V_{LR}^{(0)} = (V_1^{(0)}, 0, 0)$. In general however, the non-principal components have small but nontrivial magnitude.

To get pressure gradients $G_{DIR,k}^{(j)}$ we average p over box-shape subsets of Ω_F^r arranged symmetrically across the planes bisecting the volume Ω^r so as to obtain cell-centered approximations of P. This method of averaging was proposed in [34]; more details can be found in [33].

After averaging, for each j we have nine $V_{DIR,k}^{(j)}, k = 1, 2, 3$ and nine $G_{DIR,k}^{(j)}, k = 1, 2, 3$.

3.3.1. Computing K. For the sake of exposition, we first discuss the computation of 9 components of tensor K for Darcy model, i.e., (2.9) with $\alpha = 1, \beta = 0$. This model is a good fit for the inlet velocities in the linear laminar regime, i.e., for the first few of our experiments with $j = 0, 1, 2, \ldots$. To calculate K, we rewrite (2.9) swapping the left and right hand sides and rearranging the unknowns for clarity. For every experiment j, DIR we use $V_{DIR,k}^{(j)}$ in place of V_k and $G_{DIR,k}^{(j)}$ in place of $-\frac{\partial P}{\partial x_k}$. We have, for each $DIR = LR, TB, FB$

$$G_{DIR,1}^{(j)}K_{11} + G_{DIR,2}^{(j)}K_{12} + G_{DIR,3}^{(j)}K_{13} = V_{DIR,1}^{(j)}, \tag{3.6}$$

$$G_{DIR,1}^{(j)}K_{21} + G_{DIR,2}^{(j)}K_{22} + G_{DIR,3}^{(j)}K_{23} = V_{DIR,2}^{(j)}, \tag{3.7}$$

$$G_{DIR,1}^{(j)}K_{31} + G_{DIR,2}^{(j)}K_{32} + G_{DIR,3}^{(j)}K_{33} = V_{DIR,3}^{(j)}. \tag{3.8}$$

For each j we find the nine components of K by solving the linear system of 9 equations with 9 unknowns.

If the equations are rearranged so that all three equations for LR are followed by those for TB and finally for FB, we see that the system has a three-block diagonal

structure where all the three blocks consist of the same matrix 3×3 matrix GG

$$GG = \begin{bmatrix} G_{LR,1} & G_{LR,2} & G_{LR,3} \\ G_{TB,1} & G_{TB,2} & G_{TB,3} \\ G_{FB,1} & G_{FB,2} & G_{FB,3} \end{bmatrix}. \tag{3.9}$$

Thus (3.6)–(3.8) is solvable as long as GG is nonsingular which in turn follows if G_{DIR} are linearly independent. The latter is guaranteed in practice for the experiments with essentially orthogonal principal directions of flow.

More precisely, solving (3.6)–(3.8) we (A) calculate $K^{(j)}$ for each j so we can study its dependence on the flow rate $V^{(j)}$. Alternatively, we can (B) group together a few experiments, all with $V^{(j)}$ in the linear regime, and find K by a least squares solution to the resulting overdetermined system.

3.3.2. Computing β. The model with inertia terms generalizes (3.6)–(3.8) to the system, written for $DIR = LR, TB, FB$

$$G^{(j)}_{DIR,1} K_{11} + G^{(j)}_{DIR,2} K_{12} + G^{(j)}_{DIR,3} K_{13} - \left|V^{(j)}_{DIR}\right|^{\alpha} V^{(j)}_{DIR,1} \beta_{11} \tag{3.10}$$
$$- \left|V^{(j)}_{DIR}\right|^{\alpha} V^{(j)}_{DIR,2} \beta_{12} - \left|V^{(j)}_{DIR}\right|^{\alpha} V^{(j)}_{DIR,3} \beta_{13} = V^{(j)}_{DIR,1},$$

$$G^{(j)}_{DIR,1} K_{21} + G^{(j)}_{DIR,2} K_{22} + G^{(j)}_{DIR,3} K_{23} - \left|V^{(j)}_{DIR}\right|^{\alpha} V^{(j)}_{DIR,1} \beta_{21} \tag{3.11}$$
$$- \left|V^{(j)}_{DIR}\right|^{\alpha} V^{(j)}_{DIR,2} \beta_{22} - \left|V^{(j)}_{DIR}\right|^{\alpha} V^{(j)}_{DIR,3} \beta_{23} = V^{(j)}_{DIR,2},$$

$$G^{(j)}_{DIR,1} K_{31} + G^{(j)}_{DIR,2} K_{32} + G^{(j)}_{DIR,3} K_{33} - \left|V^{(j)}_{DIR}\right|^{\alpha} V^{(j)}_{DIR,1} \beta_{31} \tag{3.12}$$
$$- \left|V^{(j)}_{DIR}\right|^{\alpha} V^{(j)}_{DIR,2} \beta_{32} - \left|V^{(j)}_{DIR}\right|^{\alpha} V^{(j)}_{DIR,3} \beta_{33} = V^{(j)}_{DIR,3}.$$

The equations (3.10)–(3.12) have 18 unknowns: nine components of each K and β. In addition, α is either unknown or has to be assumed known. The system (3.10)–(3.12) is linear in the components of K, β, nonlinear in α, and is undetermined. We need therefore more information.

In this paper we take the approach of identifying α for each data set by trial and error. Thus we assume α is known when solving (3.10)–(3.12).

To compute β, we can proceed in one of two ways.

We can (C) first use (A) to compute $K = K^{(0)}$ for $j = 0$ from (3.6)–(3.8); i.e., we implicitly assume that $V^{(0)}$ is in the Darcy regime. Next we identify some $V^{(j)}$ in the non-Darcy regime, and set up (3.10)–(3.12), moving the now known quantities involving $G^{(j)}_{DIR,k}$ and $K = K^{(0)}$ to the right hand side. Then we solve the system for the nine components of β. The solvability of this system depends again on the structure of the block-diagonal matrix of the system which now includes the blocks

$$BB^{(j)} := - \begin{bmatrix} \left|V^{(j)}_{LR}\right|^{\alpha} V^{(j)}_{LR,1} & \left|V^{(j)}_{LR}\right|^{\alpha} V^{(j)}_{LR,2} & \left|V^{(j)}_{LR}\right|^{\alpha} V^{(j)}_{LR,3} \\ \left|V^{(j)}_{TB}\right|^{\alpha} V^{(j)}_{TB,1} & \left|V^{(j)}_{TB}\right|^{\alpha} V^{(j)}_{TB,2} & \left|V^{(j)}_{TB}\right|^{\alpha} V^{(j)}_{TB,3} \\ \left|V^{(j)}_{FB}\right|^{\alpha} V^{(j)}_{FB,1} & \left|V^{(j)}_{FB}\right|^{\alpha} V^{(j)}_{FB,2} & \left|V^{(j)}_{FB}\right|^{\alpha} V^{(j)}_{FB,3} \end{bmatrix} \tag{3.13}$$

Since these blocks are nonsingular based on the same remarks as before, the system is solvable.

Alternatively, (D) we choose two experiments j_1, j_2 and set up a system made of (3.10)–(3.12) written for each of these two experiments. In practice, we choose $j_1 = 0$ or some other j_1 in the linear regime, and vary j_2 over the nonlinear regime. The solvability is guaranteed based on a similar analysis as before. The only difficulty

may arise if j_1, j_2 are both in the linear regime so that $BB^{(j_2)}$ is merely a multiple of $BB^{(j_1)}$ by a factor of $(v_{in}^{j_2}/v_{in}^{j_1})^{1+\alpha}$.

The fit of the model (2.9) can be considered adequate if the resulting $K^{(j_1,j_2)}, \beta^{(j_1,j_2)}$ remain essentially fixed for a large range of j_2.

The results of the calculations defined above can be found in Section 4. In particular, we found that a combination of (A) and (D) was most effective.

3.3.3. Symmetry of K, β. Last but not least, the following concern arises. Clearly the tensors K, β should be symmetric but we do not enforce it when calculating these parameters from (3.10)-(3.12). The nonsymmetry however does arise in practice and is due to a combination of various numerical errors including i) the errors in pressures and velocities at microscale due to discretization and iterative solver errors, as well as ii) those in numerical averaging and iii) in solving (3.10)–(3.12) numerically, with i) being usually the most significant. Large nonsymmetry is generally an indicator for poor porescale solver performance.

If we intend to use the values of K, β in some corescale simulations, then they need to be post-processed to enforce symmetry *a posteriori*, e.g., by using the symmetric part $\frac{1}{2}(K + K^T)$ of K.

As an alternative, we can add to (3.10)–(3.12) some additional equations enforcing symmetry, e.g., requiring $K_{12} - K_{21} = 0$, etc. The enlarged system (3.10)–(3.12) thus becomes overdetermined but it can be solved by QR factorization, which is handled routinely in MATLAB.

In this paper we do not directly use K, β in corescale solvers, and therefore we report on the original and not post-processed (thus possibly nonsymmetric) tensor values.

4. Results. In this section we describe our results. First we briefly compare unstructured and structured discretizations for synthetic media because this is an issue of current interest that needs to be addressed before more complicated geometries are used. We also compare one-pore to many-pore realizations; here we restrict ourselves to synthetic 2D geometries.

Second we focus on our main objective, i.e, the 3D studies of upscaled properties of flow with a range of flow rates. We develop our methodology and test it on synthetic geometries for which we verify various common sense properties. Next we demonstrate that our methodology applies very well to voxel-based realistic pore geometries, and we identify a practical non-Darcy model based on an anisotropic power-based extension of quadratic Forchheimer model.

Given porescale flow results, i.e., the pressures and velocities, for a given flow rate $v_{in}^{(j)}$ and a particular experiment $v_{in,DIR}^{(j)}$, we calculate the average pressure gradients $G_{DIR,k}^{(j)}$ as well as velocities $V_{k,DIR}^{(j)}$ over a selected REV as discussed in Section 3.3. We also compute their magnitudes $|V_{DIR}^{(j)}|$ as well as the overall flow rate $V^{(j)} = \frac{1}{3}\sum_{DIR}|V_{DIR}^{(j)}|$ which is useful for overview of flow rates and plotting. Typically $V^{(j)}$ slightly exceeds $v_{in}^{(j)}$ which can be explained by the smallness of pore radii in the interior of Ω_F. The ratio $V^{(j)}/v_{in}^{(j)}$ grows with flow rates and with the corresponding complexity of flow profiles in tight porespace.

Given $G_{DIR,k}^{(j)}$ and $V_{k,DIR}^{(j)}, k = 1, 2, 3$, we calculate the conductivities $K^{(j)}$ as described in Section 3.3.1. As an indicator of anisotropy, we calculate

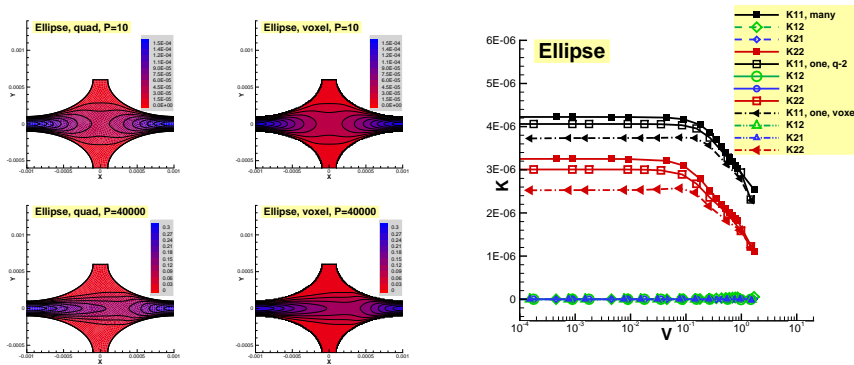$$\eta = \frac{max\{K_{mn}, m \neq n\}}{max\{K_{mm}\}} \qquad (4.1)$$

FIG. 4.1. *Illustration of simulation results for ellipsoidal synthetic region. Left: velocity magnitude profiles for small (top row) and large (bottom row) velocities; left column presents the profiles for (q) body-fitted quadrilateral grid, and the right column those for (qv) quadriletral voxel-based grid. Please note the qualitative difference between the small and large flow rates, and lack thereof between (q) and (vq) grids. Right: conductivity $K^{(j)}$.*

which measures the relative magnitude of off-diagonal components of the tensor K, and

$$\zeta = \frac{max\{|K_{mn} - K_{nm}|, m \neq n\}}{max\{K_{mm}\}} \tag{4.2}$$

which measures the relative magnitude of non-symmetry; large ζ indicates poor quality of porescale simulations and/or small REV.

4.1. 2D comparison of body-fitted and voxel grids. The motivation for this brief section on 2D geometries ties to the studies in [26, 28, 52, 18] and our earlier scaling experiments reported in [36]. In addition, the 2D results discussed here are used as a reference to our subsequent 3D simulations.

We address the following concerns. First we want to know whether for a given voxel geometry the use of structured rectangular grids leads to conductivities significantly different than those computed for a body-fitted grid using triangles or quadrilaterals.

Such a study is straightforward for a synthetic geometry. We choose here the one-pore geometry of a single pore $N_p = 1$ between solid ellipses of axes $9d \times 5d$, with $d = 10^{-4}$. For this region the periodic boundary conditions with an external pressure jump are imposed.

Second, we compare computations for many-pore region where Ω_R consists of $N_p = 9 \times 15 = 135$ pores to those with one-pore $N_p = 1$. For the many-pore geometry we use inlet-outlet boundary conditions.

The simulation results and calculated $K^{(j)}$ for the usual wide range of flow rates are shown in Figures 4.1. The data for $K^{(0)}$ is given in Table 4.1. The difference between $K^{(0)}$ values for (vq) voxel- and body-fitted discretizations (q) is above 10%, and this raises a concern. However, the values of K for (q-2) and (q-4) clearly get closer to those for (qv) when grid size h is similar; the relative difference between the results for (vq) and (q-4) is smaller than 10%.

At the same time, the differences between the results for unstructured grids with one-pore or with many-pore geometries are insignificant and within the discretization error envelope as discussed later.

N_p	grid	ϕ	$10^5 h$	$10^8 K_{11}^{(0)}$	$10^8 K_{22}^{(0)}$	$10^4 \eta$	$10^5 \zeta$
135	(t)	0.4146	2.1	422.4	325.2	2.11	15.5
1	(q)	0.4114	2.3	411.4	306.3	1.11	1.8
1	(q-2)	0.4114	1.1	406.1	300.7	0.16	0.51
1	(q-4)	0.4114	0.55	401.7	295.7	1.19	1.82
1	(vq)	0.4107	0.63	373.6	252.9	0.04	0.12

TABLE 4.1

Comparison of conductivities $K^{(0)}$ for many-pore $N_e = 9 \times 5$ and one-pore $N_e = 1$ geometries for synthetic ellipsoidal Ω_R and various grids. Here (t) refers to triangular grid, (q), (q-2), (q-4) to quadrilateral basic and refined grids, respectively, and (qv) to the structured quadrilateral voxel-based grid. Note that the differences in discretization are accompanied by slight differences in porosities.

The results are overall quite promising since they indicate that the results for body-fitted grids are comparable to those for simple quadrilateral grids. In addition, accuracy of less complex one-pore vs many-pore simulations in periodic media strongly point at the superiority of the former.

4.2. 3D porescale geometries. This section deals only with 3D data sets. For each grid listed in Table 3.2 we ran porescale flow simulations. The profiles of pressures and velocities for some simulations are illustrated in Figures 4.2, 4.3, and 4.4; note the complexity of the domain geometry and flow configurations. In Figure 4.5 we show velocity magnitude profiles for three selected flow rates for this realistic 3D data. The images show that the profiles change qualitatively with flow rate. However, unlike in synthetic 2D geometries such as in Figure 4.1, we do not think one can associate the change in a flow pattern in any individual pore unambiguously only to an increase in the flow rate in that pore or its vicinity. Rather, we believe that the observed flow patterns results from the combination of high flow rates and of viscous dissipation in a very complex anisotropic flow geometry. Recall also that the images are produced by a numerical flow solver which assumes the no-slip condition. This discussion is in contrast with regular flow patterns discussed in [5, 12] but which would be hard to reproduce in porous media with a large tortuosity.

We ran simulations with a range of inlet velocity values $v_{in}^{(j)}, j = 0, 1, \ldots^{(MAX)}$ spanning about 4-6 orders of magnitude, typically with MAX between 15 or 20. The range was designed for each data set to include certain threshold flow rates around which the qualitative nature of the porescale as well as the upscaled quantities changes.

The calculated conductivities are plotted in Figures 4.6, 4.8, 4.9. Their qualitative behavior with flow rate $V^{(j)}$ is similar to that reported in our previous studies for synthetic 2D data sets in [33] and in Section 4.1. The conductivities are approximately constant in the "slow flow" regime and they decrease past a certain threshold flow rate unique to a data set.

To support the forthcoming quantitative analyses in Tables 4.2, 4.3, and 4.4 we report the diagonal values of $K^{(j)}$ as well as $V^{(j)}$ for a few selected $j = 0, \sigma, MAX$. In addition, we provide η and ζ as measures of anisotropy and nonsymmetry. Here $j = \sigma$ corresponds approximately to the flow rate for which the principal values of K are reduced by about 1%, and past which the profiles of K begin to "curve down" as shown in Figures 4.6, 4.8, 4.9. The simulations for $j = 0$ correspond to the flow rate safe in the linear laminar regime, while $j = MAX$ to that for which we have about 50% reduction in conductivity. Another characteristic flow rate denoted by V^* corresponds to a reduction of conductivities by 10%. Since it may not necessarily

correspond to any particular $v_{in}^{(*)}$, V^* is determined by interpolation, see Section 4.4.

The conductivities $K^{(j)}$ are analyzed in detail below. In Section 4.3 we calculate the absolute permeabilities k from $K^{(0)}$ and discuss related scaling issues. In Section 4.4 we propose a non-Darcy model for $K^{(j)}$ for $j > 0$.

4.3. Conductivities $K^{(0)}$ for small flow rates. Consider first the conductivities $K^{\mathbf{D},(0)}$ in Tables 4.2, 4.3, and 4.4 obtained for different fluids, datasets, grids, voxel coarsening options, and REV parameter r, with $v_{in}^{(0)}$ chosen differently for each data set.

Absolute permeability.. For each $K^{\mathbf{D},(0)}$ we can calculate by simple scaling the corresponding absolute permeability tensor $k^{\mathbf{D}} = \mu K^{\mathbf{D},(0)}$, and we verify a few common sense properties and scaling rules that are expected to hold.

For GB and HS data sets we can compare k^{GB} and k^{HS} to the typical experimental values from literature such as in the diagram ([9], Fig. 2.4.1, Fig.4.1.7). The physical structure (glass beads) of GB is similar to that of sand and clean gravel bed of porosity $\phi \approx 0.37$. We see in Table 4.3 that $k^{GB} \approx 150d$ which is well in the range given in [9]. The porosity of $\phi^{HS} \approx 0.39$ is typical of sand/gravel rather than sandstone, and the permeability $k^{HS} \approx 8.5d$ fits well in the range $(10 - 1000)d$.

Also, we can verify the proper trivial scaling between the two fluids considered: water and methane. We recall that incompressibility was assumed; see Table 3.3 for other parameters. For example, consider $K_{22}^{B1,(0)}$ with r=0.05, see Tables 4.2. For both fluids we obtain $k_{22}^{B1} \approx 2.61d$ and the difference between the two fluid experiments is in the third significant digit only. However, for large flow rates and $j \approx MAX$ this scaling behavior does not hold; analysis will be pursued elsewhere.

Scaling with grain size.. Now consider $k^{\mathbf{D}}$ for the scaled data sets $\mathbf{D}$=B1, B1s10, B1s100, with the corresponding $d_{char}^{\mathbf{D}}$ given in Table 3.1. It is an immediate observation that the values of $K^{(0)}$ and thus also of k increase by a factor of $10^2, 10^4$ when d_{char} increases by a factor $10, 10^2$, respectively. This is consistent with the scaling $O(d_{char}^2)$ as discussed in ([9], p136) by homogenization or as follows from experimental correlations ([9], p119).

Carman-Kozeny and Collins correlations.. Now we take another look at $k^{\mathbf{D}}$ collected in Table 4.5, and which we want to compare to the permeabilities calculated with empirical formulas known from literature. In particular, we consider Carman-Kozeny correlation ([9], 4.1.20), and $k_{CK} := 0.2\frac{\phi^3 d_{char}^2}{(1-\phi)^2}$ which is given in Table 3.1. In addition, the estimate $d_{char} \approx \sqrt{\frac{k}{\phi}}$ of Collins provides a rough approximation $k_C := \phi d_{char}^2$ for k. Note that both $k_C^{\mathbf{D}}$ and $k_{CK}^{\mathbf{D}}$ are calculated using only the geometrical parameters on Ω_F^{eff} given in Table 3.1 without any flow simulations.

For a simple data set $\mathbf{D}$=B, the values $k^{\mathbf{D}}$ are close to $k_{CK}^{\mathbf{D}}$ and to $k_C^{\mathbf{D}}$. However, for $\mathbf{D}$=GB, HS, HSs, the simple correlations fail to incorporate the actual geometry of the grids, and the differences between $k^{\mathbf{D}}$, $k_C^{\mathbf{D}}$, and $k_{CK}^{\mathbf{D}}$ are large. Still, $k^{\mathbf{D}}$ falls between $k_{KC}^{\mathbf{D}}$ and $k_C^{\mathbf{D}}$ consistently for all data sets considered, so the latter can be used as lower and upper bounds for the former.

Grid convergence.. We observe in Tables 4.2, 4.3, and 4.4 that conductivity values calculated by the upscaling procedure depend, for a fixed $\Omega_F \equiv (\mathbf{n}, l)$, monotonically on the grid size. In particular, we have $K^{B1-2} > K^{B1-3} > \dots K^{B1-6}$. Generally, coarse grid results overpredict those for finer grids, e.g., $K^{HS-2-2} > K^{HS-2-3}$ and $K^{HSs-2-2} > K^{HSs-2-3}$, and $K^{GB-2-2} > K^{GB-2-3}$. The differences between coarse and fine grid values may be as high as around 10%.

$10^5 v_{in}^{(j)}$	$10^5 V$	$10^8 K_{11}$	$10^8 K_{22}$	$10^8 K_{33}$	η	ζ
B-6, r=0.05						
1	1.44	0.3571	0.3571	0.3571	(a)	(b)
1×10^4	1.44×10^4	0.3561	0.3561	0.3561	(a)	(b)
1×10^6	1.39×10^6	0.239	0.239	0.239	(a)	(b)
B-6, r=0.25						
1	1.44	0.362	0.3619	0.3619	(a)	(b)
1×10^4	1.44×10^4	0.3609	0.3609	0.3609	(a)	(b)
1×10^6	1.41×10^6	0.2479	0.2479	0.2479	(a)	(b)
B1-2, r=0.05						
1	1.56	0.3923	0.3865	0.3945	0.04	0.02
4×10^5	5.89×10^5	0.2148	0.2043	0.2131	0.04	0.02
2×10^6	2.81×10^6	0.0735	0.0679	0.0730	0.05	0.02
B1-3, r=0.05						
1	1.545	0.3204	0.3157	0.3221	0.04	0.02
4×10^5	5.91×10^5	0.1941	0.1847	0.1927	0.04	0.02
2×10^6	2.83×10^6	0.0685	0.0628	0.0678	0.05	0.01
B1-4, r=0.05						
1	1.537	0.2908	0.2865	0.2924	0.04	0.02
4×10^5	5.90×10^5	0.1819	0.1733	0.1809	0.04	0.02
2×10^6	2.83×10^6	0.0642	0.0588	0.064	0.05	0.02
B1-5, r=0.05						
1	1.533	0.2748	0.2708	0.2764	0.04	0.02
4×10^5	5.90×10^5	0.1759	0.1678	0.1753	0.04	0.02
2×10^6	2.83×10^6	0.0616	0.0565	0.0609	0.05	0.01
B1-6, r=0.05						
1	1.53	0.2652	0.2613	0.2667	0.04	0.02
4×10^5	5.89×10^5	0.1727	0.1646	0.1719	0.04	0.02
2×10^6	2.83×10^6	0.0595	0.0548	0.0591	0.05	0.02
B1-6, r=0.05, methane						
1	1.53	24.47	24.11	24.61	0.04	0.02
1×10^6	1.52×10^6	23.27	22.81	23.34	0.04	0.02
1×10^7	1.46×10^7	12.92	12.17	12.85	0.04	0.02
B1s10-6, r=0.05						
0.1	0.153	26.52	26.13	26.67	0.04	0.02
1000	1529	26.42	26.02	26.56	0.04	0.02
1×10^5	1.44×10^5	10.32	9.598	10.24	0.044	0.02
B1s100-6, r=0.05						
0.01	0.0153	2652	2613	2667	0.037	0.02
100	152.9	2642	2602	2656	0.037	0.02
1×10^4	1.44×10^4	1032	959.8	1024	0.043	0.02
B2-6, r=0.05						
1	1.643	0.1914	0.1878	0.1987	0.06	0.03
1×10^4	1.64×10^4	0.1905	0.1867	0.1975	0.07	0.03
6×10^5	9.28×10^5	0.0839	0.0741	0.0854	0.09	0.04
B3-6, r=0.05						
1	1.838	0.1323	0.1307	0.1277	0.13	0.05
4×10^5	6.87×10^5	0.0583	0.0511	0.0542	0.16	0.06
6×10^5	1.02×10^6	0.0434	0.0372	0.0399	0.16	0.06

TABLE 4.2

Conductivities for B, B1, B2, B3 computed for different grids, fluids, and with a different REV parameter r. For each data set, the first row of values corresponds to $j = 0$, the second to $j = \sigma$, and the last to $j = MAX$. We have in (a) $\eta < 10^{-5}$, and in (b) $\zeta < 10^{-6}$.

$10^5 v_{in}^{(j)}$	$10^5 V$	$10^8 K_{11}$	$10^8 K_{22}$	$10^8 K_{33}$	η	ζ
		GB-1-2, r=0.05				
1	1.14	146.9	165.7	147.6	0.06	0.02
200	228.3	146.1	164.5	147	0.06	0.03
1×10^4	1.12×10^4	85.75	93.96	87.73	0.03	0.01
		GB-1-2, r=0.25				
1	1.11	141.4	183.8	138.1	0.14	0.12
200	221	141	183.3	137.5	0.14	0.12
1×10^4	1.1×10^4	84.16	101.8	84.12	0.18	0.12
		GB-1-3, r=0.05				
1	1.14	140.1	158.6	140.6	0.06	0.02
200	228.1	138.9	157	139.7	0.06	0.03
1×10^4	1.12×10^4	82.24	90.3	84.08	0.03	0.02
		GB-1-3, r=0.25				
1	1.10	134.4	176.2	132	0.14	0.13
200	221.4	134.1	175.8	131.2	0.15	0.12
1×10^4	1.1×10^4	80.52	98.14	80.73	0.17	0.12
		GB-2-2, r=0.05				
1	1.13	165.2	183.7	171.8	0.05	0.02
200	225.6	164.3	182.6	171.1	0.05	0.02
1×10^4	1.1×10^4	88.67	95.73	96.38	0.02	0.01
		GB-2-2, r=0.25				
1	1.11	162.7	205.6	167.3	0.17	0.13
200	220.8	161.6	204.3	166.4	0.16	0.13
1×10^4	1.09×10^4	88.02	104.3	94.87	0.19	0.12
		GB-2-3, r=0.05				
1	1.13	150.6	168.4	156.7	0.05	0.02
200	224.9	149.9	167.4	156.3	0.05	0.02
1×10^4	1.1×10^4	83	89.92	90.4	0.02	0.01
		GB-2-3, r=0.25				
1	1.106	147.4	188	153.7	0.17	0.14
200	221.1	146.7	187.3	152.9	0.17	0.14
1×10^4	1.09×10^4	81.95	97.75	88.64	0.18	0.13

TABLE 4.3

Conductivities for GB computed for different grids and with a different REV parameter r. For each data set, the first row of values corresponds to $j = 0$, the second to $j = \sigma$, and the last to $j = MAX$.

For data set B1 we can attempt an estimate of the order of convergence. Consider the sequence of grids $\mathbf{D}$=B1-m with $m = 2, \ldots 6$ and the corresponding $K^{B1-m,(0)}$ with $l = l^{B1}$. We see that $K^{B1-m,(0)}$ appear to monotonically approach the finest grid value $K^{B1-6,(0)}$. This justifies the following estimate of order of convergence. We fit $\log(|K^{B1-m,(0)} - K^{B1-6,(0)}|)$ to the corresponding $\log(h_m/l)$ for the first few values $h_m/l = 1/2, 1/3, 1/4$. As a result we obtain about order 2 convergence in $K^{B1-m,(0)}$.

These analyses suggest that one could use Richardson's extrapolation to predict a more accurate $K^{\mathbf{D}}$ using only two or three refinement levels.

Repeating the same procedure for $K^{B1-m,(\sigma)}$ we see similar behavior. For $K^{B1-m,(MAX)}$ for which the porescale results are not as well resolved, the convergence order is about

$10^5 v_{in}^{(j)}$	$10^5 V$	$10^8 K_{11}$	$10^8 K_{22}$	$10^8 K_{33}$	η	ζ
		HS-2-2, r=0.05				
1	1.071	8.506	8.668	7.285	0.04	0.04
2000	2139	8.345	8.516	7.106	0.04	0.04
5×10^5	5.214×10^5	0.6852	0.7497	0.4379	0.04	0.02
		HS-2-3, r=0.05				
1	1.071	7.759	7.907	6.628	0.04	0.04
2000	2140	7.632	7.787	6.491	0.04	0.04
5×10^4	5.263×10^4	3.874	4.112	2.856	0.04	0.02
		HS-2-3, r=0.25				
1	1.12	8.557	8.46	7.178	0.06	0.03
2000	2230	8.385	8.306	7.023	0.06	0.03
5×10^4	5.399×10^4	4.091	4.299	3.053	0.04	0.04
		HSs-0-2, r=0.05				
1	1.08	4.667	4.822	4.513	0.20	0.22
2000	2162	4.566	4.719	4.415	0.19	0.21
5×10^4	5.292×10^4	2.456	2.556	2.208	0.21	0.23
		HSs-0-2, r=0.25				
1	1.204	6.291	4.377	3.75	0.22	0.22
2000	2372	6.065	4.211	3.651	0.21	0.23
5×10^4	5.596×10^4	3.13	2.366	1.948	0.32	0.33
		HSs-1-3, r=0.05				
1	1.072	4.996	5.081	4.916	0.21	0.20
2000	2141	4.906	4.992	4.82	0.19	0.20
5×10^4	5.247×10^4	2.586	2.647	2.328	0.20	0.23
		HSs-2-2, r=0.05				
1	1.06	7.537	7.171	7.306	0.18	0.17
2000	2116	7.384	7.035	7.129	0.17	0.17
5×10^4	5.178×10^4	3.597	3.436	3.071	0.18	0.20
		HSs-2-3, r=0.05				
1	1.06	6.852	6.496	6.642	0.19	0.17
2000	2121	6.738	6.393	6.51	0.18	0.17
5×10^4	5.193×10^4	3.404	3.241	2.902	0.19	0.20

TABLE 4.4

Conductivities for HS and HSs computed for different grids and with a different REV parameter r. For each data set, the first row of values corresponds to $j = 0$, the second to $j = \sigma$, and the last to $j = MAX$.

1.5.

Influence of voxel reduction.. As concerns voxel reduction levels, these are harder to compare since the data sets differ both in geometry and grid size. Overall, voxel reduction leads to higher porosity, more connectivity, and higher conductivities, as seen, e.g., by $K^{HSs-0-2} < K^{HSs-1-3} < K^{HSs-2-3}$. In addition, computations over a smaller region apparently miss some of the connectivity of a large region, hence, e.g, $K^{HSs-2-2} < K^{HS-2-2}$.

Non-symmetry, anisotropy, and REV size.. The symmetry of $K^{(j)}$ is not enforced in our computations, see the values ζ shown in Tables 4.2-4.4. Large ζ indicates poor quality of results, i.e., large numerical errors. In addition, nonsymmetry appears

D	$10^6 d_{char}^{\mathbf{D}}$	$10^{12} k^{\mathbf{D}}$	$10^{12} k_{CK}^{\mathbf{D}}$	$10^{12} k_{C}^{\mathbf{D}}$
B1	2.36	2.723	1.909	3.47
B1s10	23.6	272.3	190.86	347
B1s100	236	27,241.48	19,085.9	34,700
B2	3.07	1.88	1.20	4.94
B3	4.11	1.34	0.379	6.06
GB-1-3	11,694	1,760	367	5,120
GB-2-3	11,895	1,890	504	5,660
HSs-1-2	2.06	52.2	14.9	170
HSs-2-3	2.24	84.1	24.2	216

TABLE 4.5
Comparison of $k^{\mathbf{D}}$ and experimental correlations.

larger if REV used for averaging is small.

Generally, the values computed over a smaller REV, i.e., with $r = 0.25$ instead of $r = 0.05$, differ considerably in quality, see results for B and those for GB. Some tensor components are smaller and some are larger, and ζ as large as 20% for small REV appears unacceptable. We recommend thus to use r close to 0.

For HSs, regardless of REV size, the nonsymmetry of $K^{(j)}$ is considerable. Since HSs is a cut-out itself, the nonsymmetry is likely due to poor resolution of average pressure and velocity fields.

Last but not least, we discuss anisotropy. We see substantial anisotropy exhibited by nontrivial η in GB and HS data sets as seen in Tables 4.3 and 4.4. Anisotropy can be also clearly seen in Figures 4.8 and 4.9. It is interesting that its relative magnitude does not decrease as much with increasing velocity as we expected based on our experiments with 2D synthetic geometries in [33].

We study an anistropic model for large flow rates in what follows.

4.4. Conductivities for large flow rates and non-Darcy model. From our calculations of K, we observe a steady increase of the drag and of the resistance to flow with increasing velocity, see Tables 4.2–4.4 and Figures 4.6, 4.8, 4.9. The icreased resistance, i.e., the reduction of K, is visible starting near $v_{in}^{(\sigma)}$, and continues monotonically until v_{in} reaches the $v_{in}^{(MAX)}$. Above $v_{in}^{(MAX)}$ the porescale simulations have poor performance, and $v_{in}^{(MAX)}$ corresponds to about 50% decrease in $K^{(MAX)}$ relative to $K^{(0)}$ versus about 1% decrease corresponding to $K^{(\sigma)}$.

In Darcy's law, $K^{(j)}$ should be constant, thus a reduction of K requires a non-Darcy model. Qualitatively non-Darcy effects begin to occur around the flow rate $V^{(\sigma)}$ where we recall the reduction in K is about 1%. We are interested therefore in some threshold value of v_{in}^* and V^* for which the decrease in K^* is significant. While this is open to debate, in this paper we use as "significant" the flow rate for which the reduction in K is by about $s^* = 10\%$. This choice makes sense in numerical upscaling since K can vary by the factor s^*, e.g., when using different grids.

We declare further that a non-Darcy model is needed for flow rates in the range $(V^*, V^{(MAX)})$, and that for higher flow rates in complex media other analyses are needed. For a given data set, we can easily calculate the corresponding range $(Re^*, Re^{(MAX)})$ as the range in which non-Darcy model should be used. In fact, these critical threshold values should remain essentially the same across all data sets. We verify this

D	V^*	Re^*	$Re^{(MAX)}$	$\tilde{\alpha}$	$\tilde{\beta}$
B1	1.432	2.10	21.06	1.22	0.055
B1s10	0.1432	2.10	21.06	1.22	0.99
B1s100	0.0144	2.11	21.06	1.2	17.6
B1 methane	23.32	2.11	13.16	1.28	0.00154
B2	1.14	1.84	14.88	1.27	0.072
B3	0.866	1.27	14.97	1.35	0.084
GB	0.02	0.88	4.82	1.28	13.7
HS	0.073	0.73	5.24	1.23	2.64

TABLE 4.6

Threshold and maximal Reynolds numbers, and estimates $\tilde{\alpha}$ and $\tilde{\beta}$ of the power α and coeffcient β, respectively, obtained from fitting the non-Darcy model (2.7).
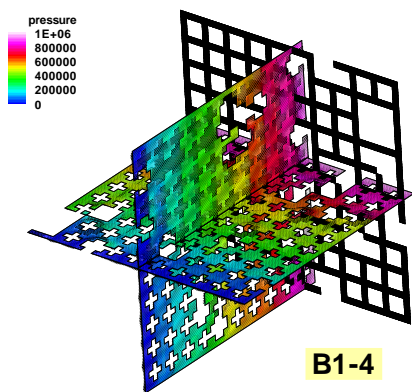
FIG. 4.2. *Pressure contours for B1-4. Slice in the back shows the geometry and grid.*

expectation below.

To identify the flow rate V^* from those in the range $V^{(j)}, j = \sigma, \dots MAX$, we use piecewise linear interpolation of $K^{(j)}$ and solve for V^*. The corresponding flux $Q^* = \phi_{eff} V^*$ and Reynolds number Re^* are calculated with (3.5), see Table 4.6. For anisotropic K we need to analyze only one of the diagonal values; here, we use K_{22}.

We see in Table 4.6 that Reynolds numbers corresponding to V^* are around 1 while those for $V^{(MAX)}$ are by about an order of magnitude higher than V^*, and around 10. This is consistent with the thresholds usually considered as the onset of non-Darcy effects. For example, in ([9], p147) Darcy's law is considered valid up to around $Re^* = 10$.

For scaled data sets such as B1, B1s10, B1s100, the threshold values Re^* remain constant. Since Re scales linearly with d_{char}, there is a similar implicit scaling of threshold values of V^* related only to the nature of flow.

Non-Darcy model.. Since $K^{(j)}$ is not constant for $V > V^{(j)}$, we see that (2.4) does not hold. We need to account for this decrease in conductivities K, i.e., propose some non-Darcy model.

We observed already in [35] for synthetic 2D data sets that extensions of (2.5) are well suited for modeling large flow rate regimes; see also [6]. In fact, it appears that there may exist several regimes of flow rates beyond merely Darcy and non-Darcy. With enough experiments and care, one can fit a particular power or polynomial
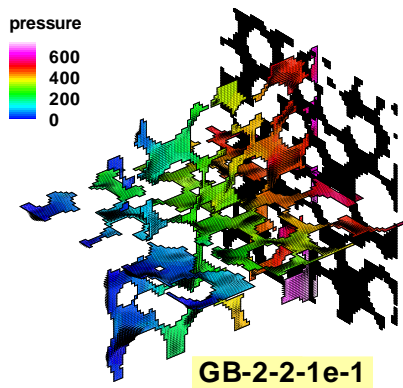
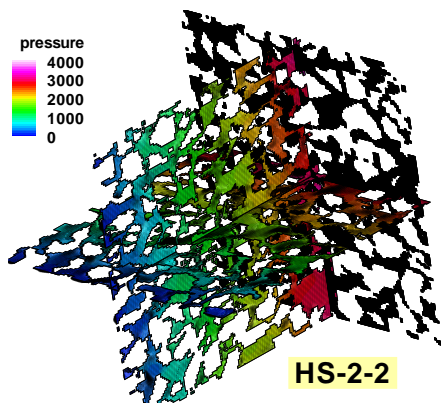Fig. 4.3. *Pressure contours for GB-2-2. Slice in the back shows the geometry and grid.*

Fig. 4.4. *Pressure contours for HS-2-2. Slice in the back shows the geometry and grid.*

model in each of these ranges of flow rates. However, in practical applications in porous media the flow rates vary; it may be difficult and unpractical to work with a flow-regime dependent model. In the analysis below we advocate finding one simple working model that can be practically implemented. Finally, any practical model needs to have a reasonable anisotropic extension.

First we consider the results for data set B for which the macroscale quantities appear isotropic as seen from η. Next we discuss data sets GB and HS which are strongly anisotropic. For each data set we use the finest grid and the least reduced voxel grid results available. Overall we find that the extended anisotropic power model (2.7) seems most adequate. The resulting approximate values of the parameters α, β are summarized in Table 4.6.

4.4.1. Isotropic non-Darcy model for B. Consider post-processed results of simulations for $\mathbf{D}$=B1-6 using method (D) from Section 3.3.2. Since the porous medium corresponding to Ω^{B1} by construction is essentially isotropic, we focus on a scalar non-Darcy law fitting one of the diagonal values of $K^{(j)}$ to $V^{(j)}$ using a polynomial or power extensions of the scalar equation (2.5).

First, we caution the reader that the quality of any fit is strongly dependent on the range of flow rates and the resolution of the data set, i.e., the number of experiments
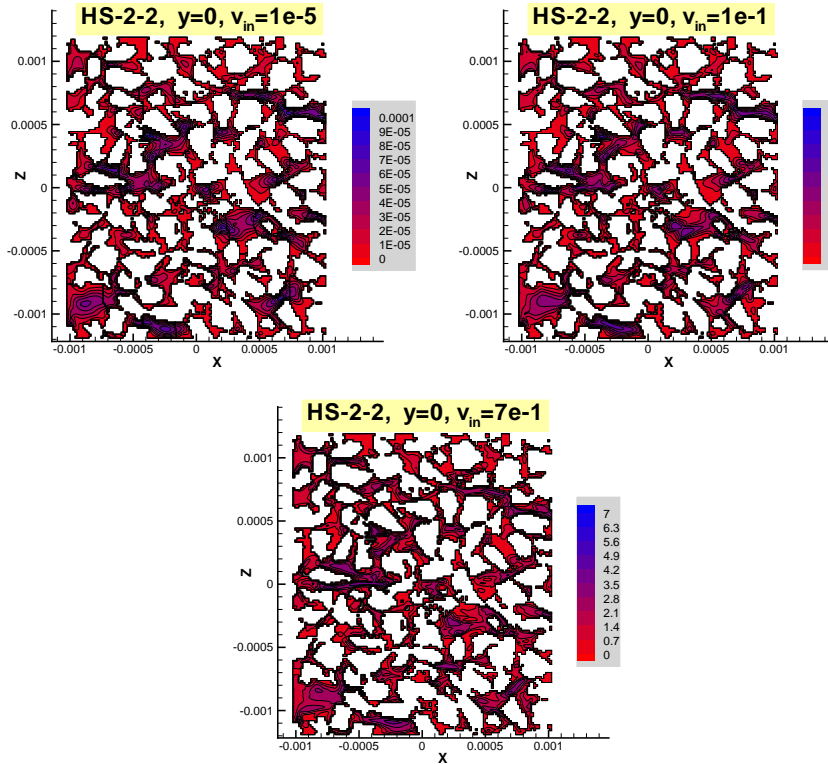
FIG. 4.5. *Velocity magnitude in a slice across HS-2-2 for* $V \approx V^{(0)}, V^*, V^{(MAX)}$, *respectively.*
Note the qualitative change with increasing flow rates, e.g., in the pore around $x = 0.005, z = -0.002$.
While these differences are clear, in general they are hard to charactertize using slices, since much
of the information on connectivity in 3D is lost.

j between V^* and $V^{(MAX)}$. In addition, a fit is only as good as the model to which
we are fitting. Finally, a proposed non-Darcy model should be not just an accurate
representation of upscaled values, but it should also be practical for implementation
of a Darcy-scale solver.

To find a plausible unique non-Darcy model for data set B1, we first calculate
tensor β using method (D) applied to (3.10)–(3.12), with $\alpha = 1$. Since we have argued
for isotropy, let us focus on β_{22} only. We notice from Figure 4.6 that β_{22} increases
with flow rates by as much as a factor of 2 in the range of flow rates $(V^*, V^{(MAX)})$.
Since β is not constant, clearly the linear Forchheimer model is not adequate.

We then attempt different functional forms for $\rho(r)$ in (2.8) with an overall
quadratic, or cubic polynomial growth, or with a simple power model (2.7). We
find that the cubic and power models provide the best fit, as shown in Figure 4.7.

However, a complete cubic polynomial model seems the least practical computa-
tionally even for isotropic media. In addition, it does not have a natural extension to
anisotropic data, as evident from our results for GB and HS data sets to be shown
below. So we settle on the power model for which we find $\alpha^{B1} \approx 1.22$. We verify
this by rerunning algorithm (D) with $\alpha^{B1} = 1.22$ to identify another set of β^{B1}, this
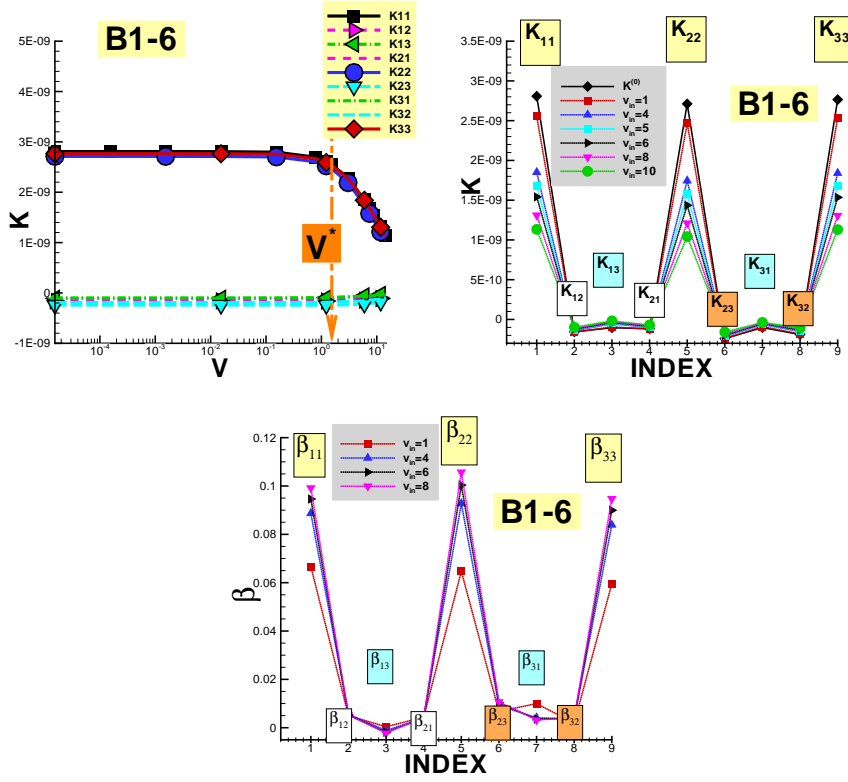time expected to be essentially constant. This is eventually confirmed as shown in
Figure 4.7.

FIG. 4.6. *Top: conductivities for a range of flow rates for B1. Middle: anisotropy and nonsymmetry in conductivities for B1. INDEX* $1, 2, 3, 4, \ldots 9$ *corresponds to the values of* $K_{11}, K_{12}, K_{13}, K_{21} \ldots K_{33}$ *arranged lexicographically as shown. Bottom: Coefficient* β *calculated with Forchheimer model for B1.*

The same calculation can be repeated for other data sets, as long as we ignore the anisotropy of K. The corresponding estimates of $\alpha^{\mathbf{D}}$ and $\beta^{\mathbf{D}}$ are shown in Table 4.6. It is interesting that the power $\alpha \in (1.2, 1.3)$ seems to fit most data sets, but that β varies significantly between the data sets. On the other hand, the results of scaling experiments for $\mathbf{D} = $B1 suggest that there is no systematic scaling of β with respect to the fluid or grain size. We defer a detailed study of β and its correlation to K to further work.

4.4.2. Anisotropic non-Darcy model for GB and HS. Now we consider GB and HS data for which clearly anisotropy occurs. We attempt a fit to the model (2.7), at first with $\alpha = 1$, and we calculate the tensor β using algorithm (D).

The resulting values of β shown in Figures 4.8 and 4.9 show that nonsymmetry and differences between the diagonal components decrease with flow rates. When fitting with a power model and $\alpha = 1$ we see also that the magnitude of the components of β is not constant across the flow rates. A set of $\alpha_1, \alpha_2, \alpha_3$ in the following modification of (2.9) may be in order

$$\sum_j \beta_{ij} |V|^{\alpha_i} V_j + V_i = -\sum_j K_{ij} \frac{\partial p}{\partial x_j}. \tag{4.3}$$
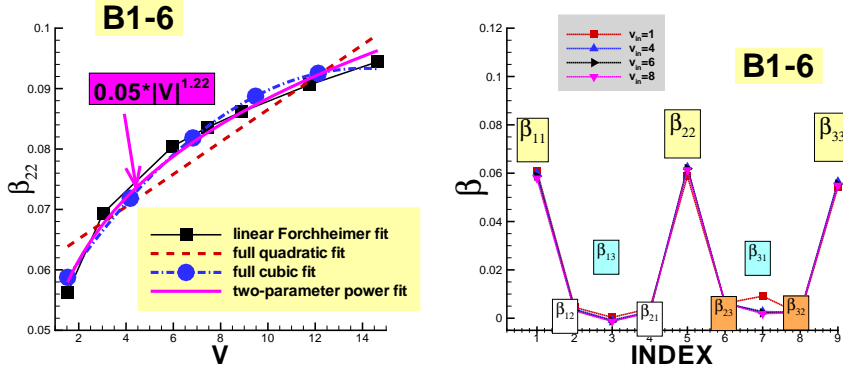
Fig. 4.7. *Top: fitting β_{22} to V with various models proposed in Section 2.1 and (2.8). The best practical fit is using $\alpha = 1.22$ and (2.7). The original data is shown as seven points (black squares) on the curve denoted as "linear Forchheimer fit". Bottom: coefficient β recalculated with non-Darcy power model and $\alpha = 1.22$ for B1. INDEX as in Figure 4.6.*

In particular, $\alpha_1 = \alpha_2 \approx 1.3$ and $\alpha_2 \approx 1.1$ gave reasonable results for $\mathbf{D}$=GB. As concerns HS, the corresponding results lead to $\alpha \approx 1.2$.

An even more complicated model than (4.3) can be sought in which $(\alpha_i)_{i=1}^3$ is replaced by a collection $(\alpha_{im})_{i,m=1}^3$. However, a macroscale implementation of (4.3) alone may be already impractical and the components α may not be possible to find experimentally.

Due to poor symmetry of results for HSs we do not have full confidence in any model fit.

4.4.3. Principal analysis of $K^{(j)}$. In this Section we discuss the anisotropic conductivities from another point of view spurred by our analyses in [33] for 2D data, where we considered behavior of principal elements of $K^{(j)}$ for a synthetic 2D data set with anisotropy. The conjecture was that the eigenvalues could be fitted to a power model and thus they would decrease with flow rates. If the eigenvectors remained stable with flow rates, one would then have a resulting simple anisotropic non-Darcy model.

Now that we have realistic 3D data set we verify this hypothesis. Its visual interpretation is most attractive if we consider 2×2 submatrices of K. Data GB is perfect for this study because the x_1 and x_3 components appear similar. Thus we extract

$$K_{2\times 2}^{(j)} := \left[\begin{array}{cc} K_{11}^{(j)} & \frac{1}{2}(K_{12}^{(j)} + K_{21}^{(j)}) \\ \frac{1}{2}(K_{12}^{(j)} + K_{21}^{(j)}) & K_{22}^{(j)} \end{array} \right], \qquad (4.4)$$

and proceed with the eigenvalue/eigenvector analysis of the symmetric part of $K_{2\times 2}^{(j)}$. Of interest are the two principal eigenvalues $e_1^{(j)}, e_2^{(j)}$ of $K_{2\times 2}^{(j)}$ and the angle ϕ that the first principal eigenvector of $K_{2\times 2}^{(j)}$ makes with the x_1 direction.

As shown in Figure 4.10, the eigenvalues decrease with flow rates as in [33]. However, the angle generally decreases with flow rates over the range $(V^{(\sigma)}, V^{(MAX)})$ and thus the conjecture postulated for syntethic media in [33] does not hold for the current complex 3D pore geometries. One can argue that this observation is consistent
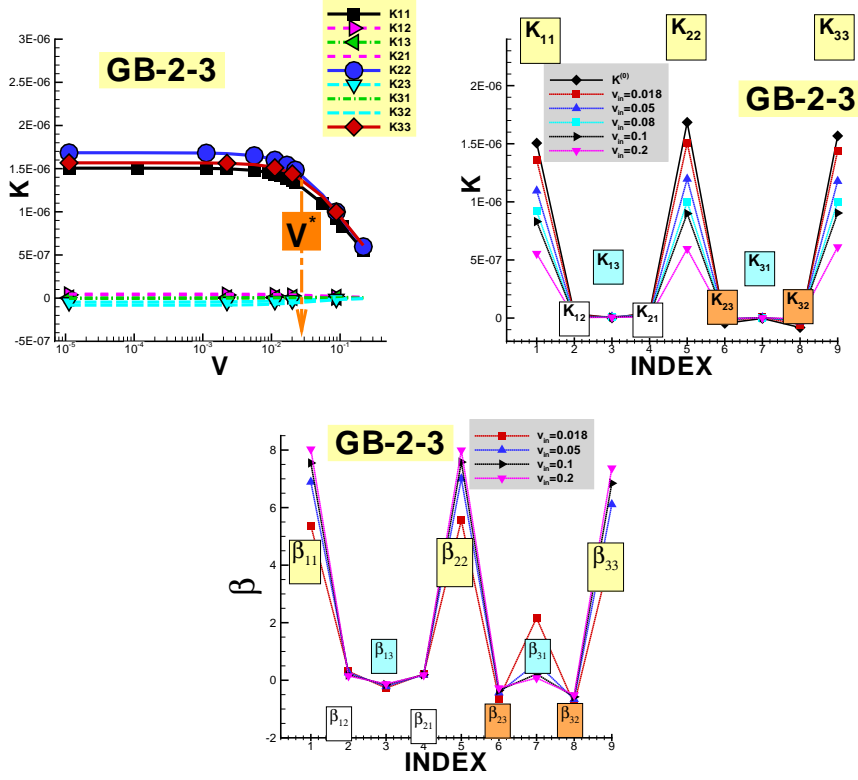
FIG. 4.8. *Top: conductivities, and middle: their anisotropy, for a range of flow rates for GB-2-3. Bottom: Coefficient β calculated with Forchheimer model. INDEX as in Figure 4.6.*

with the qualitative behavior of $K^{(j)}$ in that the tortuous paths seem straightened out with increasing flow rates, at least in the regime of flow we consider here.

5. Complexity of simulations. The computational challenges for this project include the computational time and large amount of storage space needed to save and post-process the results of simulations. Clearly, the actual computational time depends on a particular architecture used, number of processors, and other factors such as a queuing system. For reference, we provide details on the computational effort; the systems are listed at the end of this Section.

Our simulations consisted of the steps as follows.

(i) Mesh generation.. As discussed Section 3.1, our algorithms perform first various transformations of a voxel data set including voxel reductions and elimination of dead-end pores. Next we convert a voxel geometry to unstructured quadrilateral grid in a format accepted by ANSYS Fluent software.

These algorithms can generally run on a simple support workstations. However, for large meshes with $|\mathbf{n}_F| > 30 * 10^6$ cells such as GB-1-3, HS-2-3, and HSs-0-2, it is necessary to use computing nodes with large memory such as system (B).

(ii) Porescale simulations.. The simulations corresponding to each $v_{in,DIR}^{\mathbf{D},(j)}$ are clearly the most time consuming. For each simulation, the computational time grows with the size of the problem and with the number of iterations N_{it} needed to achieve assumed tolerance. Throughout all simulations we kept the tolerance fixed relative to
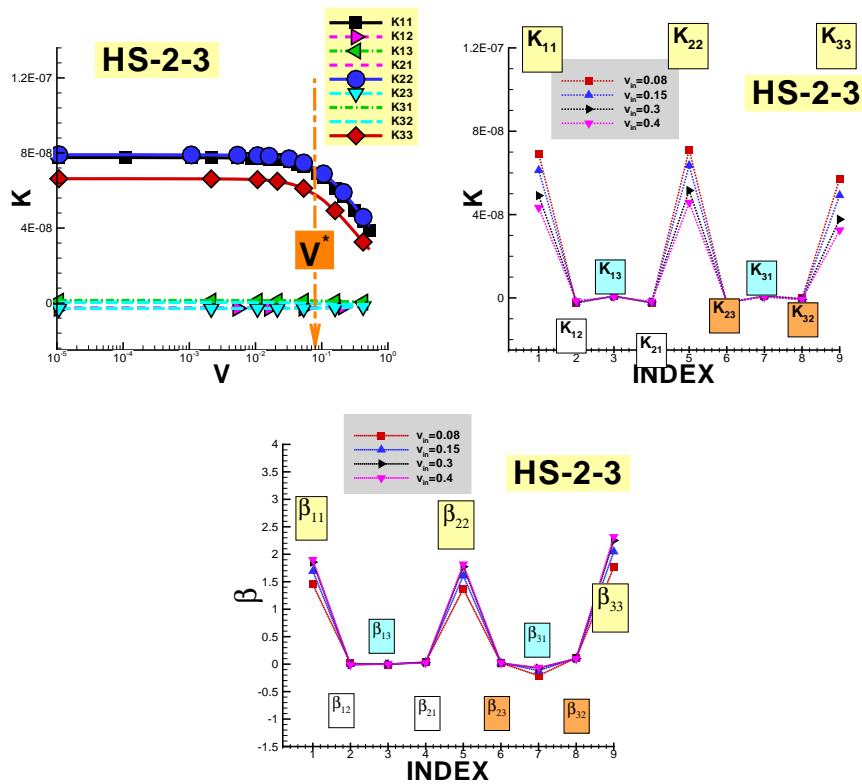
Fig. 4.9. *Top: conductivities, and middle: their anisotropy, for a range of flow rates for HS-2-3. Bottom: Coefficient β calculated with Forchheimer model. INDEX as in Figure 4.6.*
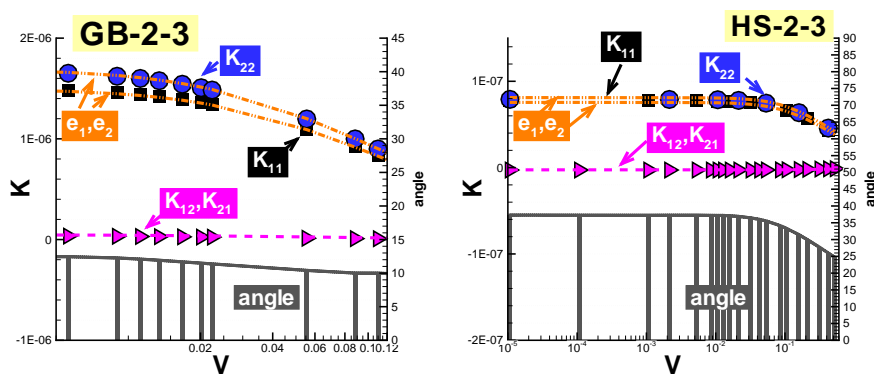

Fig. 4.10. *Principal component analysis of $K^{(j)}$: eigenvalues e_1, e_2 and angles in function of $V^{(j)}$. Each image shows simultaneously the eigenvalues (magnitude shown on the left vertical axis) and the angle formed by the principal eigenvector with the x_1 axis (magnitude shown on the right vertical axis), for a range of flow rates. The analysis is of the symmetrized $K_{2\times 2}^{(j)}$ given in (4.4). Left: analysis for GB-2-3. Right: analysis for HS-2-3.*

D	$v_{in}^{(0)}$		$v_{in}^{(MAX)}$		N_p	T_{AVE}
	N_{it}	T	N_{it}	T		
B1-2	40	0:01	66	0:02	8 (C)	0:02
B1-6	157	0:14	213	0:18	64 (C)	0:52
B1s100-6	157	0:15	213	0:19	64 (C)	0:52
B2-6	149	0:12	205	0:15	64 (C)	0:44
B3-6	135	0:08	221	0:12	64 (C)	0:35
GB-1-2	231	4:16	357	1:30	48 (B)	0:42
GB-1-3	362	1:08	606	1:42	128 (C)	2:37
GB-2-2	137	0.04	143	0:05	48 (B)	0:06
GB-2-3	198	0:36	246	1:03	48 (B)	0:29
HS-2-2	140	0:11	170	0:12	64 (C)	1:07
HS-2-3	283	0:55	289	0:53	64 (C)	3:29
HSs-0-2	456	1:31	798	2:18	96 (C)	3:21
HSs-1-2	215	0:06	338	0:09	64 (C)	0:27
HSs-1-3	276	0:38	582	0:58	64 (C)	1:27
HSs-2-2	125	0:01	140	0:01	32 (C)	0:04
HSs-2-3	183	0:04	241	0:05	32 (C)	0:12

TABLE 5.1

Complexity of simulations for pressure outlet boundary condition and selected $V_{in,BT}^{(j)}$. N_{it} is the number of iterations needed, T is the wall-clock time (in hours), and N_p is the number of processors used on a given HPC system.

a characteristic velocity magnitude for a given case. The number N_{it} depends on the complexity of geometry of **D** and grows with the flow rate. To obtain well-resolved porescale results with small ζ, we applied very stringent convergence tolerance criteria.

Generally, the simulations for flow rates in $v_{in}^{(0)}, v_{in}^{(\sigma)})$ require fewer iterations than those for $j > \sigma$. On the other hand, the appearance of nonlinear effects in $K^{(j)}, j > \sigma$, is accompanied by a visible increase in N_{it} and in a growing number of outlet boundary faces where the recirculation occurs. For the flow rates above $V_{in}^{(MAX)}$ the solver is sometimes unable to find the solution within the desired tolerance.

(iii) Post-processing step.. In this step, all porescale results are averaged and collected in a form convenient for upscaling and for further analysis as decribed in 3.3. We compute averaged velocities $V_{DIR,k}^{(j)}, k = 1, 2, 3$ and pressure gradients $G_{DIR,k}^{(j)}, k = 1, 2, 3$ and analyze them typically for a few values of r characterizing REV size. Much of post-processing is done on one of the original computing nodes since the data from multiprocessor runs has to be collected from the local disk space. The approximate time T_{ave} of averaging for one REV is given in Table 5.1. Note that T_{ave} is actually considerable compared to T.

(iv) Analysis, visualization, and non-Darcy models.. The final computations such as solving (3.10)–(3.12) and the fitting of non-Darcy models is done in MATLAB which has an abundant set of appropriate tools. The computational complexity was negligible compared to (i)-(iii).

HPC systems.. In Table 5.1 we provide detailed report on the computational complexity. For (ii)-(iii) we used exclusively the facilities of ICM, University of Warsaw as follows. System (A) was used for testing various grids, geometries, and boundary conditions, and systems (B)-(C) were used for production runs.

(A) x86 cluster Halo2, Sun Constellation 6048 System based on AMD Quad-Core Opteron 835X nodes x86_64 architecture.
(B) x86 cluster Hydra, HP BladeSystem/Actina based on AMD Opteron 2435/Intel Xeon 5660/AMD Opteron 6132 nodes x86_64 architecture, nodes with 24/32/256 GB of memory.
(C) Power 775 IBM Supercomputer Boreasz, architecture based on Power7 supernodes.

6. Discussion, conclusions and future work. The main goal of this paper has been to demonstrate that computational simulations at porescale as well as the proposed upscaling and parameter identification methodologies work well for realistic pore geometries over a substantial range of flow rates.

As an outcome of our pore-to-core methodology, we proposed a practical new anisotropic non-Darcy flow model based on a power extension of Forchheimer model with a power $\alpha \approx 1.2$, and with an anisotropic tensor coefficient β. The values of β need further study since they vary considerably between geometries; some analyses in this direction are underway.

We performed various studies with the voxel based data sets and various grids as well as for a large range of flow rates. Several of our findings are unsurprising and are summarized as follows. Solver performance deteriorates significantly with i) increasing $|\mathbf{n}|$, ii) decreasing porosity, and iii) increasing complexity of pore space, iv) increasing flow rates, and v) decreasing h. For each dataset there is an upper (or lower) limit on each of these parameters beyond which simulations are not reliable and converged solutions are very hard to obtain.

The calculated conductivity values vary depending on the computational mesh, on the degree to which the original voxel data set was transformed, as well as on the REV size. The differences may be as high as 20%. On the other hand, we found that difference in conductivities between body-fitting grids and voxel-based grids are about 10%, depending on grid size. Overall it is desirable, if at all possible, to use grids resolved enough so that relative difference in conductivities between refinement levels is around 1-2%. As a good indicator of quality of results, one should assess symmetry of the resulting tensors. Large nonsymmetry indicates poor solver performance and/or REV that is too small.

Overall, a departure from linear laminar model is apparent both from pointwise fluid properties at porescale and from study of corescale conductivities. The onset of inertia effects identified as 1% reduction in conductivities K value correlates with the sudden decrease of solver performance.The regime up to which flow simulations proceed reliably corresponds to reduction of K about 50%.

Since the values of K depend so much on the grid and other simulation parameters, there arises a natural question of the regime where non-Darcy effects should be considered significant enough to warrant the need for a flow model extending Darcy's. As a rule of thumb, we propose to consider the discrepancy from Darcy model significant when the conductivities are reduced by around 10% which occurs for flow rate dubbed V^*. This reduction factor is on par with the differences due to different discretizations.

The flow rate V^* corresponds to a Reynolds number specific to a data set but generally close to $Re^* \approx 1$. For coupled flow and transport models when the flow rates are about an order of magnitude smaller than Re^* we still advocate the use of a model with inertia effects at corescale and/or porescale. This is because inertia has a distinct qualitative if not quantitative impact on fluid behavior which may affect

transport properties. This aspect is part of our ongoing work.

More studies are needed for more complex geometries, realistic scenarios, and macroscopically heterogeneous media. These studies need to identify, e.g., how to handle flow systems with flow rates which are large only locally. In addition, it would be desirable to compare computational studies directly with experimental data for the same porous sample. In particular, we hope to be able to contribute and compare our methodology within the porescale benchmarking project [1].

REFERENCES

[1] Porescale Benchmark. In: www.porescalebenchmark.pbworks.com/
[2] Akjani, L., Matthai, S.: Finite element-based characterization of pore-scale geometry and its impact on fluid flow. Transport in Porous Media **81**, 241–259 (2010)
[3] Andrade, J.S., Costa, U.M.S., Almeida, M.P., Makse, H.A., Stanley, H.E.: Inertial effects on fluid flow through disordered porous media. Phys. Rev. Lett. **82**(26), 5249–5252 (1999). DOI 10.1103/PhysRevLett.82.5249
[4] ANSYS, Inc.: ANSYS FLUENT User's Guide, Rel. 14.0 (2011)
[5] Balhoff, M., M.F.Wheeler: A predictive pore-scale model for non-darcy flow in porous media. SPE J. **14**, 579–587 (2009)
[6] Balhoff, M., Mikelic, A., Wheeler, M.: Polynomial filtration laws for low Reynolds number flows through porous media. Transport in Porous Media **81**, 35–60 (2010)
[7] Bear, J.: Dynamics of Fluids in Porous Media. Dover, New York (1972)
[8] Bear, J., Bachmat, Y.: Introduction to modeling of transport phenomena in porous media. Kluwer (1990)
[9] Bear, J., Cheng, A.: Modeling Groundwater Flow and Contaminant Transport. Springer (2010)
[10] Bourgeat, A., Marusić-Paloka, E., Mikelić, A.: Weak nonlinear corrections for Darcy's law. Math. Models Methods Appl. Sci. **6**(8), 1143–1155 (1996)
[11] Cai, R., Lindquist, W., W.Um, Jones, K.: Tomographic analysis of reactive flow induced pore structure changes in column experiments. Advances in Water Resources **32**, 1396–1403 (2009)
[12] Chaudhary, K., Cardenas, M., Deng, W., Bennet, P.: The role of eddies inside pores in the transition from Darcy to Forchheimer flows. Geophysical Research Letters **38**, L24,405 (2011). DOI doi:10.1029/2011GL050214
[13] Chen, Z., Lyons, S.L., Qin, G.: Derivation of the Forchheimer law via homogenization. Transp. Porous Media **44**(2), 325–335 (2001)
[14] Chu, J., Engquist, B., Prodanovic, M., Tsai, R.: A multiscale method coupling network and continuum models in porous media i: Steady-state single phase flow. Multiscale Modeling & Simulation **10**(2), 515–549 (2012). DOI 10.1137/110836201. URL `http://epubs.siam.org/doi/abs/10.1137/110836201`
[15] Dullien, F.: Porous media. Academic Press San Diego (1979)
[16] Ergun, S.: Fluid flow through packed columns. Chemical Engineering Progress **48**, 89–94 (1952)
[17] Ewing, R.E., Lazarov, R.D., Lyons, S.L., Papavassiliou, D.V., Pasciak, J., Qin, G.: Numerical well model for non-Darcy flow through isotropic porous media. Comput. Geosci. **3**(3-4), 185–204 (1999)
[18] Finn, J., Apte, S.: Relative performance of body-fitted and fictitious-domain simulations of flow

through porous media. Procededings of the ASME Fluids Engineering Summer Meeting (FEDSM2012-72355) (2012)

[19] Forchheimer, P.: Wasserbewegung durch Boden. Zeit. Ver. Deut. Ing. (45), 1781–1788 (1901)

[20] Fourar, M., Lenormand, R., Karimi-Fard, M., Horne, R.: Inertia effects in high-rate flow through heterogeneous porous media. Transport in Porous Media **60**, 353–370(18) (2005). DOI doi:10.1007/s11242-004-6800-6

[21] Fourar, M., Radilla, G., Lenormand, R., Moyne, C.: On the non-linear behaviour of a laminar single-phase flow through two and three-dimensional porous media. Advances in Water Resources **27**, 669–677 (2004)

[22] Garibotti, C., Peszyńska, M.: Upscaling non-Darcy flow. Transport in Porous Media **80**, 401–430 (2009). DOI DOI10.1007/s11242-009-9369-2

[23] Giorgi, T.: Derivation of Forchheimer law via matched asymptotic expansions. Transport in Porous Media **29**, 191–206 (1997)

[24] Hassanizadeh, S.M., Gray, W.: High velocity flow in porous media. Transport in Porous Media **2**, 521–531 (1987)

[25] Huang, H., Ayoub, J.: Applicability of the Forchheimer equation for non-Darcy flow in porous media. SPE Journal **(SPE 102715)**, 112–122 (2008)

[26] Koivu, V., Decain, M., Geindreau, C., Mattila, K., Bloch, J.F., Kataju, M.: Transport properties of heterogeneous materials. combining computerised x-ray micro-tomography and direct numerical simulations. International Journal of Computational Fluid Dynamics **23**(10), 713–721 (2009)

[27] Marusić-Paloka, E., Mikelić, A.: The derivation of a nonlinear filtration law including the inertia effects via homogenization. Nonlinear Anal. **42**(1, Ser. A: Theory Methods), 97–137 (2000)

[28] Masad, E., Muhunthan, B., Martys, N.: Simulation of fluid flow and permeability in cohesionless soils. Water Resources Research **36**(4), 851–864 (2000)

[29] Mattis, S., Dawson, C., Kees, C., M.W.Farthing: Numerical modeling of drag for flow through vegetated domains and porous structures. Advances in Water Resources **39**, 44–59 (2012)

[30] Mei, C.C., Auriault, J.L.: The effect of weak inertia on flow through a porous medium. J. Fluid Mech. **222**, 647–663 (1991)

[31] Narsilio, G., Buzzi, O., Fityus, S., Yun, T., Smith, D.: Upscaling of Navier-Stokes equations in porous media: Theoretical, numerical and experimental approach. Computers and Geotechnics **36**, 1200–1206 (2009)

[32] Patankar, S.V.: Numerical Heat Transfer and Fluid Flow FLUENT software. (Hemisphere, Washington DC (1980)

[33] Peszyńska, M., Trykozko, A.: Convergence and stability in upscaling of flow with inertia from porescale to mesoscale. International Journal for Multiscale Computational Engineering **9**(2), 215–229 (2011). DOI 10.1615/IntJMultCompEng.v9.i2.60

[34] Peszynska, M., Trykozko, A., Augustson, K.: Computational upscaling of inertia effects from porescale to mesoscale. In: G. Allen, J. Nabrzyski, E. Seidel, D. van Albada, J. Dongarra, P. Sloot (eds.) ICCS 2009 Proceedings, LNCS 5544, Part I, pp. 695–704. Springer-Verlag, Berlin-Heidelberg (2009)

[35] Peszyńska, M., Trykozko, A., Kennedy, K.: Sensitivity to anisotropy in non-Darcy flow model from porescale through mesoscale. In: Proceedings of CMWR XVIII in Barcelona, June 21-24, 2010. available online at http://congress.cimne.com/CMWR2010/Proceedings (2010). URL `http://congress.cimne.com/CMWR2010/Proceedings/docs/p46.pdf`. Paper 46

[36] Peszyńska, M., Trykozko, A., Sobieski, W.: Forchheimer law in computational and experimental studies of flow through porous media at porescale and mesoscale. In: Mathematical Sciences and Applications, *Current Advances in Nonlinear Analysis and Related Topics*, vol. 32, pp. 463–482. GAKUTO Internat. Ser. Math. Sci. Appl. (2010)

[37] Porter, M., Schaap, M., Wildenschild, D.: Lattice-Boltzmann simulations of the capillary pressure- saturation-interfacial area relationship for porous media. Advances in Water Resources **32**, 1632–1640 (2009)

[38] Renard, P., Genty, A., Stauffer, F.: Laboratory determination of the full permeability tensor. Journal of Geophysical Research **106**(Bll), 26,443–26,452 (2001)

[39] Ruth, D., Ma, H.: On the derivation of the Forchheimer equation by means of the averaging theorem. Transport in Porous Media **7**(3), 255–264 (1992)

[40] Sánchez-Palencia, E.: Nonhomogeneous media and vibration theory, *Lecture Notes in Physics*, vol. 127. Springer-Verlag, Berlin (1980)

[41] Schaap, M., Porter, M., Christensen, B., Wildenschild, D.: Comparison of pressure-saturation characteristics derived from computed tomography and lattice Boltzmann simulations. Water Resour. Res. **43**(W12S06) (2007)

[42] Scheidegger, A.E.: The physics of flow through porous media. Revised edition. The Macmillan

Co., New York (1960)

[43] Smolarkiewicz, P., Winter, C.L.: Pores resolving simulation of darcy flows. Journal of Computational Physics **229**, 3121–3133 (2010)

[44] Sobieski, W., Trykozko, A.: Sensitivity aspects of Forchheimer's approximation. Transport in Porous Media **89**, 155–164 (2011)

[45] Succi, S.: The lattice Boltzmann equation for fluid dynamics and beyond. Numerical Mathematics and Scientific Computation. The Clarendon Press Oxford University Press. Oxford Science Publications

[46] Tartakovsky, A., Meakin, P.: Pore scale modeling of immiscible and miscible fluid flows using smoothed particle hydrodynamics. Advances in Water Resources **29**, 1464–1478 (2006)

[47] Tartakovsky, A., Scheibe, T., Meakin, P.: Pore-scale model for reactive transport and biomass growth. Journal of Porous Media **12**, 417–434 (2009)

[48] Tartar, L.: Incompressible fluid flow in a porous medium–convergence of the homogenization process. In: Nonhomogeneous media and vibration theory, *Lecture Notes in Physics*, vol. 127, pp. 368–377. Springer-Verlag, Berlin (1980)

[49] Wesseling, P.: Principles of computational fluid dynamics, *Springer Series in Computational Mathematics*, vol. 29. Springer-Verlag, Berlin (2001)

[50] Wodié, J.C., Lévy, T.: Correction nonlinéaire de la loi de Darcy. C. R. Acad. Sci. Paris Sér. II Méc. Phys. Chim. Sci. Univers Sci. Terre **312**(3), 157–161 (1991)

[51] Zaman, E., Jalali, P.: On hydraulic permeability of random packs of monodisperse spheres: Direct flow simulations versus correlations. Physica A **389**, 205–214 (2010)

[52] Zaratskiy, Y., Geiger, S., Sorbie, K., Foerster, M.: Efficient flow and transport simulations in reconstructed 3d pore geometries. Advances in Water Resources **33**, 1508–1516 (2010)